A tonically active neuron continuously drives mutually exclusive motor states at different timescales

Jun Meng[1,2], Tosif Ahamed[2]*, Bin Yu[3], Wesley Hung[2], Sonia EL Mouridi[4,5], Zezhen Wang[6], Yongning Zhang[3], Quan Wen[6], Thomas Boulin[4], Shangbang Gao[3], Mei Zhen[1,2]*

1. Department of Physiology, University of Toronto, Toronto, ON, Canada
2. Lunenfeld-Tanenbaum Research Institute, Mount Sinai Hospital, Toronto, ON, Canada
3. Huazhong University of Science and Technology, Wuhan, China
4. Univ Lyon, Université Claude Bernard Lyon 1, MeLiS, CNRS UMR 5284, INSERM U1314, Institut NeuroMyoGène, Lyon 69008, France
5. King Abdullah University of Science and Technology (KAUST), Biological and Environmental Science and Engineering Division (BESE), KAUST Environmental Epigenetics Program (KEEP), Thuwal, 23955-6900, Saudi Arabia
6. School of Life Sciences, University of Science and Technology, Hefei, Anhui, China

Abstract

Behaviors consist of distinct states and state transitions. How a neural system continuously modulates each state, which underlies smooth state transitions, is not well understood. *C. elegans* spontaneously switches between two mutually exclusive motor states, forward and backward movements, a behavior long thought to reflect the reciprocal antagonism between interneurons that separately gate the forward and backward motor circuits. We report here that during spontaneous locomotion, these interneurons are not functionally equivalent, and are not strictly reciprocally inhibitory. Instead, AVA, the premotor interneuron thought to exclusively gate the backward motor circuit, functions as a master regulator for both motor states. AVA's transient activation inhibits the forward circuit while initiating backward movement. In parallel, AVA maintains a constitutive and excitatory input to the forward circuit to promote the exit from backward movement and to maintain forward movement. This excitation results from AVA's sustained depolarized membrane potential, which makes its chemical synapse tonically active. A tonically active master neuron breaks the symmetry between the forward and backward motor circuit, and offers an elegant circuit solution for smooth transitions when animals switch between two mutually exclusive motor states.

Introduction

Behaviors are often considered as sequences of discrete motor states. Some states, such as the forward and backward movements, are mutually exclusive[1–11]. Circuit structures such as the winner-take-all and reciprocal inhibition represent a few general solutions that select and promote distinct states[12–16].

However, at shorter timescales, behaviors are less discrete and are more accurately represented as continuously modulated variables, such as the velocity for locomotion[3,17–20]. This is particularly evident when animals switch between mutually exclusive motor states. Indeed, growing experimental evidence show that the neural network's activity is continuously modulated in behaving animals[21]. Circuit mechanisms for continuous modulation that underlies smooth transitions between mutually exclusive states are not well understood.

We address this question using the *C. elegans* model system. *C. elegans* exhibits two mutually exclusive motor states: forward movement and backward movement, propelled by the posteriorly and anteriorly propagating undulatory bending waves, respectively. In the absence of explicit sensory stimuli, animals spontaneously switches between the two states[22].

The transition between forward and backward movements has been described by a reciprocally inhibitory neural model: two modules, one for forward movement and one for backward movement[23,24], function separately[25–29]; synaptic connectivity regulates the transition rate and dwell time in each module[6]. This model treats the forward and backward states as mirrored modules; transitions from one to another occur stochastically or through an external input bias.

Previous measurements of *C. elegans* locomotion have revealed additional features not captured by above model. Examples include the continuous decay of forward velocity prior to the transition into backward movement, the period of post-stimulus arousal, during which animals

exhibit a higher than pre-stimulus velocity after they exit an escape response[30], and the puzzle that reducing the activity of premotor interneurons of the backward module decreases not only the backward but also forward velocity[31].

Here we revisit the relationship between the forward and backward motor circuit during spontaneous locomotion. Anatomically, two groups of non-spiking premotor interneurons, AVB and AVA, make dominant inputs onto two groups of motor neurons that separately execute the forward and backward movements[23,24]. Their functions have been considered to be 'dedicated', with AVB promoting forward motor circuit and AVA gating backward motor circuit[25–29].

However, through experimental and modeling studies, we found that AVA and AVB are not functionally equivalent and are not strictly reciprocally inhibitory. Instead, AVA, the premotor interneuron that gates the backward motor circuit, has a constitutive and excitatory input on AVB, which activates forward movement. This allows AVA to not only inhibit the forward circuit when it activates the backward movement, but also activate the forward circuit to promote exit from reversals and sustain forward movement. Hence AVA functions as a master neuron to sustain locomotion when the animal switches between the forward and backward movements.

These results allude to a fundamental asymmetry in the motor circuit that operates with two mutually exclusive motor states. We draw above conclusion from following studies.

First, our whole-cell patch clamp recording revealed that AVA maintains a strongly depolarized membrane potential, whereas AVB does not. A non-spiking neuron's activity is sensitive to membrane potential changes. Manipulation of endogenous K^+ leak leads to controlled perturbation of neuronal activity. When we induced a further depolarization of AVA by decreasing its K^+ leak, both forward movement and backward movement are potentiated, whereas with a moderate hyperpolarization, both motor states are potently inhibited. These effects were not mirrored by AVB.

These findings prompted us to evaluate the relationship between AVA and AVB when animals spontaneously locomote. Calcium and behavioral data from wild-type animals fit a simple model: a fast and inhibitory input with a delayed positive input from AVA can predict both AVB activity and velocity. This model fits the calcium and behavioral data when AVA was further depolarized, but fails when AVA was moderately hyperpolarized. These results postulate that AVA can inhibit and potentiate AVB at different phases of locomotion, an effect that requires AVA to maintain a depolarized membrane potential.

These results are consistent with the previous observation that chemogenetic inactivation of AVA reduces overall velocity, but contradict the previous observation that optogenetic activation of AVA locks the animal in into the backward motor state. With an optogenetic stimulation protocol that mimics constitutive depolarization, we confirmed that increased AVA activity potentiates overall velocity. With the behavioral effect of chemogenetic inhibition that mimics a sequential hyperpolarization of AVA, we obtained further support on AVA's opposing effect on the forward motor circuit: while AVA's transient depolarization, which initiates backward movements, inhibits forward movement, in parallel, AVA maintains a positive input on the forward circuit to promote forward movement. Through cell and synapse ablation, we showed

that AVA potentiates the forward circuit through constitutive acetylcholine release. Thus, by maintaining depolarized membrane potential, AVA maintains an excitatory input onto the forward circuit while gating the backward motor circuit.

Our study leads to an alternative model. Instead of operating as two equivalent and opposing modules, a tonically active master neuron breaks the symmetry by regulating both mutually exclusive motor states. A master neuron provides a circuit solution for continuous modulation of velocity during spontaneous transitions between mutually exclusive states.

This master neuron belongs to the backward circuit, a module more frequently evoked during escape, a behavior essential for survival. Under ambient laboratory conditions, *C. elegans* favors forward over backward movement. It makes economic sense for a neural system to make use of the tonic activity of a neuron, primed to execute escape, to support forward locomotion.

Results

AVA maintains a more depolarized membrane potential than AVB

AVA and AVB do not fire all-or-none action potentials. Instead, their membrane potentials fluctuate in an analog fashion[6,32,33]. Instead of choosing the lowest potential at an arbitrarily estimated steady state as the 'resting' potential, we represent their membrane potentials by the range, as well as the dynamic change. The range is shown by cumulative distribution (Fig. S1A), and the dynamics by the joint probability distribution of the membrane potential and its time derivative (Fig. 1S1B).

Quantification of our AVA whole-cell patch clamp recording supports the previous conclusion [34–36] that AVA maintains a depolarized potential at multiple stable states. AVA's potential ranged from approximately -30 mV to -10 mV (median -23mV) (Fig. 1F; Fig. 1SA). Its fluctuation exhibits two regimes with small time derivatives, one from -30 mV to -20 mV, the other from -15mV to -10mV (Fig. 1S1C).

In contrast, our recording of AVB revealed a membrane potential at more hyperpolarized range, approximately from -75mV to -10mV (median -57mV) (Fig. 1S1A). AVB also exhibited dynamic changes in different stable states, most prominently from -75 mV to -45mV (Fig. 1S1B).

AVA's membrane properties are consistent with the notion that AVA could remain active even when it's at baseline. At baseline, AVA's potential is near the opening threshold of UNC-2[37], a synaptic high voltage-gated calcium channel that promotes vesicular release[38–40].

An endogenous K^+ leak current regulates AVA's membrane potential

To understand why AVA is tonically depolarized, we examined the consequence of changing its membrane potential.

A neuron's membrane potential can be manipulated by changing its inward and outward leak currents (Fig. 1A). We identified TWK-40, a predicted K2P channel for K^+ leak (Methods; Fig. 1B). Endogenously tagged (Fig. 2S1A) and fully functional (Fig. 2S1B) TWK-40::TagRFP was

more abundantly expressed in three neuron classes, AVA, AVB, and DVA, with AVA expression level higher than others (Fig. 1C). TWK-40::TagRFP is present at plasma membrane, at the soma and enriched along the neurite (Fig. 1C).

TWK-40 forms a functional K^+ leak channel (Fig. 1D). Exogenous expression of TWK-40 in the HEK293T cells led to a small increase of their outward leak current (Fig. 1Di, ii), similar to a few mammalian K2P channels [41–43]. A gain-of-function (gf) form, which carries a mutation (L181N) that universally increases K2P channel activity [44,45], led to a large increase in the outward leak current that depends on the intracellular K^+ (Fig. 1Di, iii). TWK-40 forms a functional K^+ leak channel (Fig. 1D). In HEK293T cells, exogenous expression of TWK-40 led to a small increase of the cell's outward leak current (Fig. 1Di, ii), similar to some exogenously reconstituted wild-type K2P channels [41–43]. A gain-of-function (gf) form of TWK-40(L181N), which carries a mutation that universally increases K2P channel activity [44,45], led to a large increase in the outward leak current (Fig. 1Di, iii). Decreasing K^+ concentration in the intracellular solution eliminated the increase of TWK-40(gf)-mediated leak current (Fig. 1Di, iii).

We introduced the loss-of-function (lf*)* and gain-of-function (gf*)* mutations in *C. elegans twk-40* genomic locus (Fig. 1B; Methods). As expected, AVA exhibited a decreased and increased outward leak current in *twk-40(lf)* animals (Fig. 1E). Consistent with the effect of K^+ leak, AVA's membrane potential became further depolarized in *twk-40(lf)* (~-25mV to 0mV), and hyperpolarized (-40mV to -10mV) in *twk-40(gf)* animals (Fig. 1F; Fig. 1S1C). AVA-specific restoration of TWK-40 led to increased outward leak current (Fig. 1E) and hyperpolarization (Fig. 1F; Fig. 1S1C).

AVA activity is controlled by its membrane potential

Genetic manipulation of the membrane potential allows for controlled activity perturbation of non-spiking neurons. Indeed, in freely-moving *twk-40(lf)* and *twk-40(gf*) mutants, AVA exhibited increased and decreased overall calcium signals, respectively (Fig. 1S2A). Moreover, consistent with the opposing effects of the inward Na^+ leak and outward K^+ leak currents on membrane potential, genetic mutations that lead to an increased Na^+ leak (*nca-1(gf)*) partially restored the diminished AVA's calcium signal in *twk-40(gf)* mutants (Fig. 1S2B).

With cell-type specific manipulation of TWK-40 activity, below we investigate the physiological consequence of AVA's depolarized membrane potential, in context of the intact motor circuit and spontaneous locomotion.

Depolarization of AVA potentiates both backward and forward movements

In the absence of explicit sensory stimuli, wild-type animals spontaneously switch between forward and backward movements (Fig. 2A). *twk-40(lf)* mutants exhibit more frequent transitions into the backward motor state, prolonged reversals, and increased body bending during both reversals and forward movement (Fig. 2B, C). These changes suggest an increase in the animal's overall motor activity.

To assess which neurons contribute to the increased motor activity, we degraded endogenous TWK-40 proteins from sub-groups of TWK-40-expressing neurons using a repurposed ubiquitin-

ligase system[46] (Methods; Fig. 2S1A, B). Depleting TWK-40 from AVA alone was sufficient to recapitulate overall increased motor activity (Fig. 2B, C; Fig. 2S1D), while depletion of TWK-40 from AVB, DVA, or other neurons had no effect (Fig. 2S1D). When we restored TWK-40 specifically to AVA in *twk-40(lf)* animals, body bending during both forward and backward movements was restored to wild-type levels (Fig.2S1C). Consistently, AVA exhibited increased calcium activity with AVA-specific depletion of TWK-40 (AVA-TWK-40*(*lf*)*), as in *twk-40(lf)* mutants (Fig. 2S2C).

These results were unexpected. Considered as 'dedicated' to the backward motor circuit, AVA should either explicitly regulate the backward circuit, or exert opposite effects on the backward and forward circuits. To further evaluate its role in forward movement, we abolished the animal's ability to reverse by ablating the motor neurons that execute reversals, the A-MNs (Methods). Forward movement was not significantly changed in these animals[25]; However, further ablation of AVA led to significant attenuation of forward movement (Fig. 2S2Ai). In *twk-40(lf)* mutants, co-ablation of AVA and A-MNs similarly reduced their forward movement (Fig. 2S2Aii).

AVA's depolarization potentiates backward as well as forward motor circuit activity.

Hyperpolarization of AVA decreases both backward and forward movement

Mirroring our observation with the *twk-40(lf)* mutants, the *twk-40(gf)* mutation exerts similar effect for both forward and backward motor states. *twk-40(gf)* mutants exhibit reduced motor activity, with a slightly stronger effect on reversals: forward movement was drastically reduced, and backward movement was abolished (Fig. 2B, C). Furthermore, with AVA-specific TWK-40(gf) expression, AVA's calcium activity was drastically reduced (Fig. 2S2C), and overall motor activity was reduced, with a slightly stronger effect during backward movement (Fig. 2B, C).

These defects could not be explained by a potential developmental effect of hyperpolarization. Applying an acute, optogenetic silencing of AVA with GtACR2 (Methods), we also observed similarly silenced forward and backward movement (Fig. 2S2B).

Together, AVA's depolarized membrane potential sustains the animal's motility, not only during backward but also forward movements.

AVA's potentiation of forward movement requires AVB

To investigate the circuit mechanism that underlies AVA's potentiation on forward movement, we examined the effect of ablating neurons that have been implicated in either potentiating forward locomotion (AVB, PVC)[27,47] , or, partitioning the forward and backward motor states (RIM)[48–53] (Fig. 3S1A).

Consistent with previous reports[27,54,55], ablation of AVB significantly reduced forward movement (Fig. 3A). More importantly, ablating AVB in AVA-specific TWK-40(lf) mutants significantly reduced forward movement (Fig. 3B). AVB ablation did not further attenuate the forward movement in AVA-specific TWK-40(gf) mutants, or upon optogenetic hyperpolarization of AVA (Fig. 3S1B, C). Ablation of other neurons - PVC and RIM - did not

attenuate the forward movement of either wild-type animals (Movie S1) or *twk-40(lf)* mutants during spontaneous locomotion (Fig. 3S1A; Movie S2).

These results suggest that AVA potentiates forward movement in part through AVB, the dominant premotor interneuron of the forward motor circuit.

AVA positively regulates AVB's activity

To examine how AVA regulates AVB's activity, we directly assessed the amplitude of dynamic change of AVB's membrane potential upon perturbation of AVA (Fig. 3C; Fig. 3S2A).

In wild-type animals, AVB's membrane potential fluctuates between -75mV to -10mV (median -55mV) (Fig. 3S2B, wild-type). When AVA was further depolarized, AVB exhibited a significant increase in the amplitude of potential changes (Fig. 3C; Fig. 3S2A, AVA-TWK-40(lf)), which might correlate with a more depolarized membrane potential range (~-50mV to -10mV, median -32mV) (Fig. 3S2B, AVA-TWK-40(lf)). Conversely, when AVA was hyperpolarized, the dynamic range of AVB's membrane potential changes was drastically reduced (Fig. 3C; Fig. 3S2A, AVA-specific TWK-40(gf)) and a slight hyperpolarization in the potential range (~-75mV to -30mV, median -58mV) (Fig. 3S2B, AVA-specific TWK-40(gf)).

Consistently, in freely moving animals, AVB's mean calcium activity showed a corresponding increase and decrease when AVA was further depolarized (Fig. 3D, AVA-specific TWK-40(lf)) and hyperpolarized (Fig. 3D, AVA-specific TWK-40(gf)), respectively.

Together, AVA's depolarized membrane potential positively regulates AVB, the premotor interneurons that potentiate forward movement.

A predominant communication from AVA to AVB

These results revealed an unexpected, non-antagonizing input from AVA to AVB. We asked whether this effect was reciprocal, specifically, whether AVB might also potentiate AVA.

We examined the effect of AVB inhibition on the backward motor circuit. As expected, optogenetic silencing of AVB reduced the forward movement in moving animals (Fig. 4A; Fig. 4SA) and decreased AVB's calcium activity in immobilized animals (Fig. 4SC). In these animals, backward movement was unchanged (Fig. 4A; Fig. 4SA), and AVA's activity pattern was similar with or without AVB silencing (Fig. 4C).

The lack of an effect of AVB silencing on AVA contrasted with the effect of AVA silencing on AVB. Consistent with the notion that AVA positively regulates AVB's membrane potential and calcium activity, optogenetic inhibition of AVA led to attenuated forward movement in moving animals (Fig. 2S2B; Fig. 4B), and reduced calcium activity in both AVA and AVB (Fig. 4D; Fig. 4S1D).

These results reveal a more complex relationship between AVA and AVB. Instead of a strict reciprocal inhibition, these experimental findings – AVA's depolarized membrane potential maintains both backward and forward motor states, whereas AVB specifically potentiates the forward state – implicate an asymmetry between the forward and backward motor circuits. During spontaneous locomotion, communication is predominantly from AVA to AVB.

A two-timescale model predicts AVA's regulation of AVB activity

These results raised the need to directly examine the relationship between AVA and AVB neuronal activity, which had not been simultaneously analyzed in freely moving animals[6,26,56]. We performed simultaneous calcium imaging of AVA and AVB during spontaneous locomotion and examined their relationship (Methods).

For both neurons, the largest activity transients occurred during motor state transitions. As reported[26,27,56–61], each epoch of AVA transients aligned with a transition event. Specifically, the initiation of a reversal coincided with the onset of AVA's calcium rise, whereas the exit from a reversal coincided with the onset of AVA's calcium decay (Fig. 5SA). During this period, AVB's calcium change was anti-correlated with that of AVA (Fig. 5B; Fig. 5SB).

This relationship changed after animals began an exit from the reversal. While AVA's activity rapidly decayed to a steady baseline, AVB showed a continued rise as the animal exited the reversal, followed by a slow decay after the animal entered forward movement (Fig. 5B; Fig. 5SA). AVA maintained its baseline calcium signals during subsequent forward movement (Fig. 5B; Fig. 5SA).

We sought the simplest mathematical model that describes this dynamical relationship. Because the functional communication between the two neurons was largely unidirectional (Fig. 4), we considered an input/output model where AVA is treated as the input to AVB. The calcium imaging data suggested a model with two timescales: a fast input during reversals, and a slower one during post-reversals, to account for two phases of AVB activity dynamics. This led to a simple linear dynamical system model (Fig. 5A).

$$x_{AVB} = a \cdot x_{AVA} + b \cdot y \qquad (1)$$

$$\frac{dy}{dt} = -\frac{1}{\tau} \cdot y + x_{AVA} \qquad (2)$$

where x_{AVB} and x_{AVA} represent the activity of AVB and AVA, respectively; y represents the slow input from AVA (1), given by the leaky-integrator in (2). The model has three free parameters: strength of the fast input a, strength of the slow input b, and the timescale for the slow input τ.

We used the framework of linear systems identification to fit parameters to our calcium imaging data (Fig. 5A; Methods). The best-fit parameters set the strength of fast input a to a negative value, and the slow input b to a positive value (Fig. 5D).

Biologically, this could be interpreted as the forward circuit receiving a fast and inhibitory input and a slow excitatory input from AVA at different timescales. In other words, AVA maintains a constitutive and excitatory input on AVB, in addition to a strong activation-mediated inhibitory to AVB during transitions. Without the slow excitatory input, the gradual decay of AVB activity after a reversal cannot be predicted by the one timescale model (Fig. 5B, C).

With different parameter values, this two-timescale model could also predict the animal's spontaneous velocity from AVA's activity (Fig. 5Gi). Therefore, this model is capable of explaining the continuous modulation of behavior during behavioral transitions.

Together, these results suggest a new model: AVA functions as a master regulator of spontaneous locomotion by bi-directional regulation of AVB at different timescales. A transient but strong depolarization of AVA leads to phasic inhibition during reversals, while a persistent but weak depolarization of AVA provides tonic excitation to AVB that promotes forward movement between reversals (Fig. 5H).

Depolarized membrane potential is necessary for AVA's master regulator role

We asked if AVA's master regulator role requires AVA to maintain its membrane potential. We co-imaged AVA and AVB in freely behaving AVA-specific TWK-40(lf) and AVA-specific TWK-40(gf) mutants, and examined their relationships.

When we further depolarized AVA (AVA-TWK-40(lf)), the time-dependent relationships with AVB and velocity (Fig. 5SBii; 5SDii) are maintained. The two-timescale model predicted AVB's activity (Fig. 5B-D) and velocity (Fig. 5Gii) from AVA's calcium signals. Parameters for both inputs showed a trend of further increase, but with a slightly higher value for the fast input a (Fig. 5D). Biologically, this suggests that with further depolarization, AVA maintains and strengthens both fast-inhibitory and slow-excitatory inputs (Fig. 5D; Fig. 5SDii).

In AVA-TWK-40(gf) mutants, the relationship between AVA and AVB activity changed completely such that the model was no longer applicable. Both neurons exhibited drastically reduced calcium signals with little dynamical changes (Fig. 2B, C; Fig. 5SAiii). In rare cases where AVA exhibited detectable calcium transients, AVB tracked these changes (Fig. 5E, F), but these transients were not correlated with specific motor states (Fig. 5SCiii).

These results suggest that the two-timescale model for AVA's master regulator role is contingent on its depolarized membrane potential.

A constitutive, minimal optogenetic depolarization of AVA potentiates the forward circuit

Our results reveal AVA's dual modulation – transient inhibition and constitutive excitation – of the forward circuit. Previous optogenetic depolarization of AVA resulted in instantaneous initiation and sustenance of reversals[55,62]. We reasoned that currently stimulation protocol only reflects AVA's inhibitory effect of the forward circuit upon strong depolarization (Fig. 6A).

To mimic constitutive, weak excitation, we applied a new stimulation protocol to a strain that expresses Chrimson specifically in AVA (Fig. 6B; Methods). Specifically, we pre-conditioned the AVA neuron through a period of activation before we subjected animals to a constitutive and minimal light stimulation. These animals recapitulated the motor pattern of AVA-TWK-40(lf) mutants – more frequent transitions and potentiation of both forward and backward movements (Fig. 6B, '+ Con, +ATR'). Without pre-conditioning (Fig. 6B, '- Con, +ATR'), this stimulation increased reversal frequency without potentiating forward movement. Without the co-factor that activates Chrimson (Fig. 6B, '+ Con, -ATR'), light alone did not potentiate either motor state. Further supporting that AVA positively regulates AVB activity, in the absence of AVB, this stimulation protocol no longer potentiated the forward movement (Fig. 6S, '-AVB').

This result corroborates our conclusion that AVA maintains a weak, but constitutive excitatory input onto the forward motor circuit.

Chemogenetic hyperpolarization of AVA isolates potentiation of forward movement
A constitutive input from AVA may reflect a tonic activation of its synaptic activity. We examined this possibility through dosage-dependent chemogenetic hyperpolarization by a histamine-gated chloride channel (HisCl)[31].

Exposing animals that ectopically express HisCl in AVA led to a histamine-dependent reduction of reversals, as well as spontaneous forward speed[31]. We further noted that the backward motor circuit exhibited higher sensitivity to histamine (Fig. 6C, D). At 2mM, histamine nearly fully blocked reversals (Fig. 6C) while only modestly reduced forward movement (Fig. 6D). With increased histamine, forward movement progressively declined (Fig. 6D). An implication of this result is that with gradual membrane hyperpolarization, AVA rapidly loses its ability of transient activation hence the transient inhibitory input onto the forward circuit, but gradually loses its constitutive and excitatory effect on the forward circuit.

To directly visualize the effect of HisCl on AVA's synaptic activity, we examined the intensity of synaptobrevin/SNB-1::pHluorin, a marker of synaptic vesicle exocytosis[63] along the AVA axon (Fig. 6F; Methods). As expected from increased and decreased vesicular release, *twk-40(lf)* and *twk-40(gf)* mutants exhibited an increased and decreased steady-state fluorescent intensity, respectively (Fig. 6F). In wild-type animals, histamine-induced AVA hyperpolarization led to a dosage-dependent progressive decrease of SNB-1::pHluorin signals (Fig.6E). These results are consistent with a gradual attenuation of synaptic vesicle release as AVA becomes increasingly hyperpolarized. Importantly, at lower histamine concentrations, which blocked reversals with modest effects on forward movement, SNB-1::pHluorin signals were reduced but remained.

Together, our genetic, optogenetic, and chemogenetic perturbation of AVA's membrane potential consistently demonstrate AVA's dual modulation of the forward motor circuit: in addition to a transient inhibition during reversals, AVA maintains constitutive excitation which is likely through constitutive synaptic activity.

Tetanus toxin selectively blocks AVA's chemical synaptic transmission
We asked whether AVA's transient and constitutive inputs are mediated through different forms of synaptic transmission. AVA forms both chemical and electrical synapses with other neurons [23,26,63,64]. For chemical synaptic transmission, AVA functions primarily as a cholinergic neuron, but also synthesizes multiple neuropeptides [65–67].

By cleaving synaptobrevin/SNB-1, tetanus toxin (TeTx) is commonly used to block exocytosis hence chemical synaptic transmission[68,69]. Prior to applying TeTx to block AVA's chemical synaptic transmission, we first asked whether TeTx impairs both synaptic and dense core vesicle exocytosis, which underlie classic neurotransmitter release and neuromodulator secretion, respectively.

We addressed this question by comparing TeTx's effect on a synaptic vesicle marker (SNB-1::GFP) (Fig. 7A) and two neuropeptide markers[70], INS-22::pHluorin (Fig. 7B) and INS-22::GFP (Fig. 7C), all expressed in AVA. TeTx, specifically expressed by AVA, diminished the SNB-1::GFP signals at AVA's presynaptic termini (Fig. 7A). In contrast, TeTx did not change the steady-state signals of INS-22::pHluorin, a proxy for dense-core vesicle exocytosis (Fig. 7B).

INS-22::GFP signals were increased along AVA's axon (Fig. 7Ci), but were similarly accumulated in the scavenger cell for secreted peptides (Fig.7Cii).

These results indicate that at least in the AVA neuron, TeTx potently blocks synaptic vesicle release, but has only a minor effect on neuropeptide secretion. This allowed us to attribute effects of specific expression of TeTx in AVA (below) to an impaired chemical synaptic transmission.

Cholinergic transmission underlies AVA's constitutive excitation of the forward circuit
AVA-TeTx led to significant decreases of both forward and backward movements, in both wild-type animals and *twk-40(lf)* mutants (Fig. 8S1). AVA is cholinergic. We further compared the effect of reducing vesicle loading of acetylcholine by AVA-specific RNA interference (RNAi)[71] against an acetyltransferase CHA-1 (Methods)[72]. Similar to AVA-TeTx, AVA *cha-1* RNAi led to a reduction of both forward and backward movements (Fig. 8A, Fig. 8S1). Lastly, TeTx fully blocked AVA-mediated potentiation of forward movement upon constitutive and minimal optogenetic stimulation (Fig. 8B). These results demonstrate that AVA's potentiation of the forward motor circuit requires cholinergic synaptic transmission.

Consistent with its behavioral effect, TeTx disrupted AVA's dynamic relationships with AVB (Fig. 8C). In AVA-TeTx animals, AVA continued to exhibit activity calcium transients; however, AVB's activity transient was drastically reduced (Fig. 8S2A, B), disrupting the correlation between AVA and AVB calcium dynamics (Fig. 8C). Occasionally, AVB exhibited activity transients that did not correlate with AVA. Neither AVA or the rare AVB calcium dynamics showed correlations with velocity (Fig. 8S2A).

We conclude that AVA's acetylcholine release contributes to both constitutive activation and transient inhibition of the forward motor circuit (Fig. 8D). Critical for this study is a requirement for AVA's tonic cholinergic transmission to potentiate forward movement. The simplest implication is that AVA's strongly depolarized membrane potential supports constitutive vesicular release of acetylcholine, providing a slow but continuous positive driving force for the forward motor circuit to ensure smooth motor state transitions.

Discussion

Our study investigates how a neural system continuously modulates different behavioral states to aid their transitions (Fig. 8D). *C. elegans* spontaneously transits between forward and backward movements. Despite their mutual exclusion, the two motor states are not independently controlled. Two groups of premotor interneurons separately gate the motor neurons that execute either forward or backward movements, but these interneurons do not strictly antagonize each other. Instead, AVA, the interneuron that gates motor neurons for reversals, regulates AVB, the interneuron that activates motor neurons for forward movement, at two timescales and with opposite polarities. When AVA activates the reversal motor neurons, a fast but transient inhibitory input to AVB promotes the backward movement. Simultaneously, AVB receives a slow but tonic excitatory input from AVA, which allows transitions from reversals into sustained forward movement. Mechanistically, AVA's tonic excitatory input results from a depolarized membrane potential, which supports constitutive acetylcholine release. This configuration breaks the structural and functional symmetry between the forward and backward motor circuit, making

AVA the master regulator of both states. A tonically active master neuron offers an elegant circuit solution for continuous behavioral modulation.

Forward and backward motor states are asymmetric

C. elegans intrinsically transits between the forward and backward motor states, but these two states are not mere mirrored functional modules.

During spontaneous locomotion, *C. elegans* preferentially sustains forward movement over backward movement, resulting in a higher propensity of the forward state. But when executed, the shorter backward movement exhibits greater rigor than forward movement[73].

Reversal is frequently evoked and prolonged when animals encounter repulsive stimuli and attempt escape[73]. Importantly, evoked reversals reveal its potent modification of the forward motor state that follows. A prolonged reversal more likely activates turning, a form of forward movement that steers away from the original trajectory. A shorter reversal more likely resumes forward movement with a similar trajectory, which resembles most spontaneous reversals[74] Evoked reversals further increase the forward speed that follows, potentiating the forward state up to several minutes[75].

Reversal thus represents an intrinsically more robust, but actively suppressed motor state; its activation modifies and potentiates the subsequent forward state. Our studies examine neural mechanisms that underlie this inherent asymmetry.

Forward and backward motor states are not separately controlled

Anatomically, the forward and backward motor circuit consists of distinct sets of motor neurons and premotor interneurons wired with mixed electrical and chemical synapses. Despite similarity in their wiring configuration, the two motor circuits are not symmetric modules.

Neurons that drive backward movement have higher excitability. Premotor interneuron AVA maintains a depolarized membrane potential at ~ -23mV, contrasting a significantly hyperpolarized potential of the premotor interneuron of the forward circuit (~-55mV). Excitatory motor neurons that execute reversals have higher spontaneous activity than those of forward movement[25,27]. These differences corroborates the intrinsic robustness of reversals.

Neurons of the backward motor also play the more dominant role in the overall motor control. While the two motor states are separately executed by motor neurons in each circuit[25,29] (this study), they are not separately regulated by premotor interneurons. AVB is more dedicated, promoting the forward state. AVA promotes both motor states. When depolarized, AVA initiates reversals. When at its 'rest' state, it generates tonic, positive drive for AVB to promote forward movement. AVA being a master regulator aligns with the modification of the forward motor state after evoked reversals.

AVA underlies continuous modulation of motor activity

A master neuron that bi-directionally regulate two mutually exclusive motor states aids spontaneous transitions.

Previously, we and others showed that AVA exerts dual modulation of the backward motor circuit[25,26,52]. At its 'rest' state, AVA reduces spontaneous reversals by gap junction-mediated shunting the motor neurons that execute reversals. At its activated state, AVA initiates reversals via chemical synapse-mediated potentiation of these motor neurons. Here, we show that AVA's chemical synapses exert dual modulation of the forward circuit. At its 'rest' state, AVA steadily potentiates the forward motor circuit through a tonic release of acetylcholine. At its activated state, AVA transiently inhibits the forward circuit.

These are complementary effects for overall motor control: when AVA is at 'rest', the forward motor state is stabilized by simultaneous inhibition of the reversal and activation of the forward circuit. When AVA is activated, the backward motor state is promoted by simultaneous activation of the reversal and inhibition of the forward circuit (Fig. 8D).

Central to AVA's role is its depolarized membrane potential with a mixed wiring configuration. Being intrinsically depolarized, its gap junctions actively suppress the backward motor state, while its intrinsic excitability allows for phasic, but robust reversals. Being tonically depolarized, a baseline release from its chemical synapses slowly but tonically potentiates forward movement. With opposing effects on both motor circuits at different timescales, AVA underlies continuous modulation of both motor states.

Our model is derived from spontaneous locomotion. The proposed configuration, with minimal feedback from AVB, likely represents a minimal functional module. When sensory inputs impose changes to locomotion, reciprocal feedbacks between AVA and AVB might be recruited to modify the relationship between forward and backward movement. However, the inherent asymmetry between the two motor states should always impose a more dominant effect from the reversal motor circuit.

Premotor interneurons of the reversal circuit regulate an overall motor activity

It is interesting that premotor interneurons of the backward, not forward circuit, play the dominant role in overall motor control. Reversals are driven by a robust but actively suppressed circuit. The motor system finds an economical solution by using the same tonic drive to shunt backward and potentiate forward locomotion. This solution allows animals to generate robust escape responses. Moreover, AVA's tonic input to AVB, an integrated copy of its activity with slow decay, might serve as a short-term memory of the history of internal state and environment.

Discrepancies between anatomic and functional connectivity

AVA's regulation of the forward circuit cannot be directly deduced from the anatomical wiring. In the wiring diagram, AVA does not make stereotypic direct synaptic inputs to AVB, whereas AVB makes stereotypic synaptic inputs to AVA[23,76,77].

There are several potential explanations. The simplest is that AVA's synaptic connections with other interneurons relay its effects on AVB, but this seems unlikely. The wiring diagram offers two candidates, RIM and PVC, that connect the forward and backward motor circuit. Indeed, our ablation of RIM or PVC led to an increased spontaneous reversal, an effect consistent with RIM-

specific chemical synapse ablation[47,50,52,78], but these animals maintain coordinated forward-backward transitions and spontaneous velocity. Their ablation did not reduce the overall motor activity in *twk-40(lf)* mutants either.

We favor the mechanism that AVA's tonic acetylcholine release facilitates extra-synaptic accumulation and potentiation of the forward motor circuit. Indeed, in the developing larvae, extrasynaptic cholinergic transmission from premotor interneurons provides tonic potentiation of ventral muscles that functionally substitute for the missing ventral bending motor subcircuit[79].

A systematic survey of functional connectivity upon single neuron optogenetic stimulation revealed extensive discrepancies between anatomic chemical synaptic wiring and functional connectivity throughout the *C. elegans* nervous system[80,81] . A partial correlation between anatomic wiring and correlated neuronal activity patterns has been similarly noted in other systems[82–85].

Other forms of functional communication - ephaptic coupling, extrasynaptic transmission, modulatory signaling – might compensate for the small number of anatomy wiring in a small neural system. However, the more interesting postulation from this study is that these 'invisible' wiring is utilized for spontaneous behavioral states, and the anatomic wiring, such as AVB to AVA, is preferentially recruited for evoked behavioral responses – another economical form of wiring.

Dynamic regulation of a non-spiking neuron network

With a few exceptions[86,87], The *C. elegans* neural system consists primarily of non-spiking neurons[32,34,55,63,86,88–92]. This network generates behavioral outputs that share dynamic properties of other animals: stable, flexible, and adaptive, largely disposed of regenerative potentials.

AVA's functional model suggests that a precise and dynamic regulation of neuronal activity can be achieved through precise modulation of membrane potentials. Fine-toning individual neuron's membrane potential determines the form of this neural network. An exceptional expansion of potassium channels, in particular, the 47 K^+ leak channels[44,93–95] might serve this need. *C. elegans* neurons function through graded membrane potential changes[32,35,36,88–90,92,96]. Such electrical characteristics are particularly suited for K2P currents to determine a neuron's range and form of responses to stimuli[93,97]. With 47 K2P genes expressed by overlapping subgroups of 300 neurons [66], they might serve as a combinatorial code to differentiate each neuron of the entire nervous system.

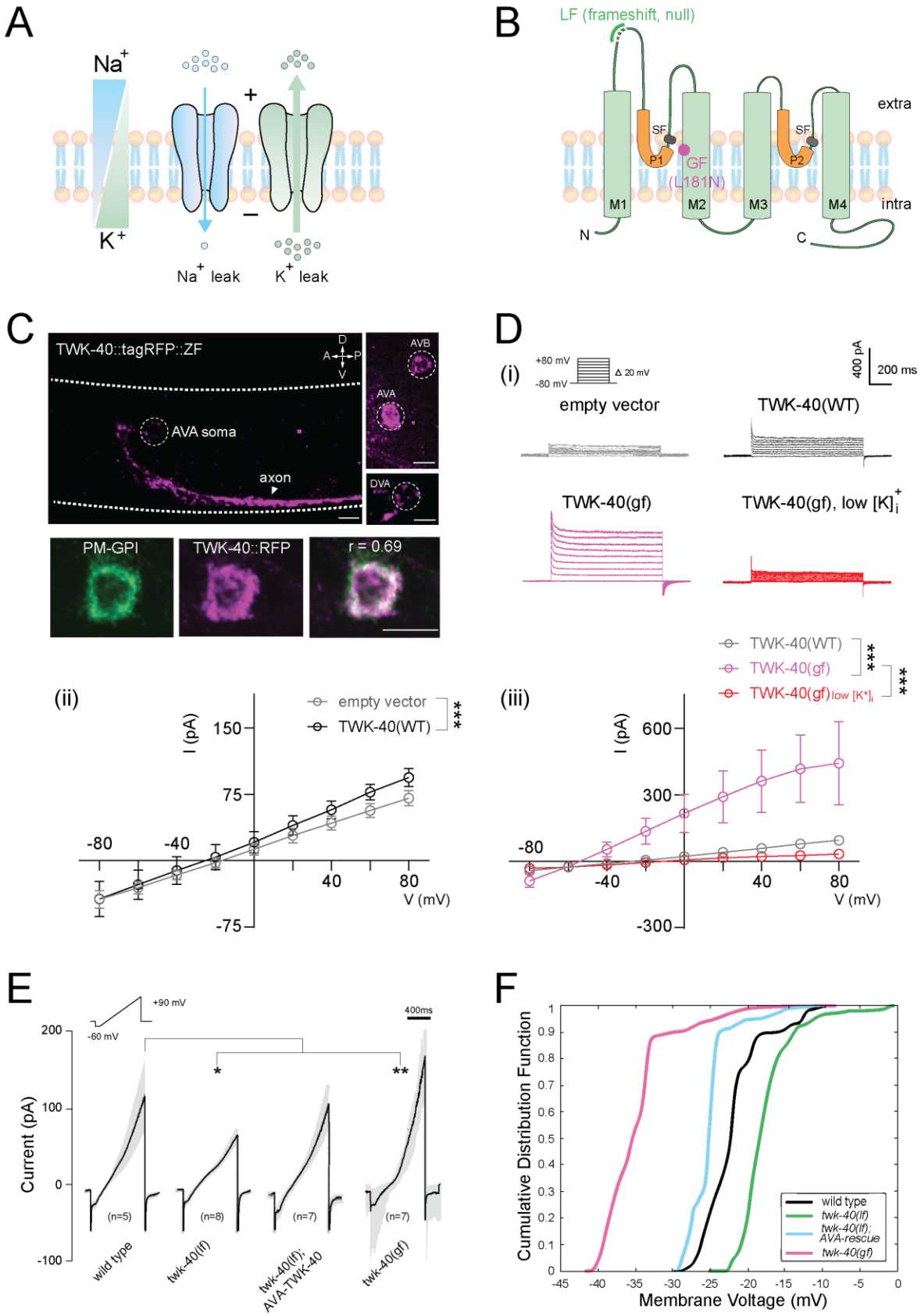
A
Na+
K+
+
−
Na+ leak
K+ leak
B
LF (frameshift, null)
extra
intra
SF
P1
P2
GF
(L181N)
M1
M2
M3
M4
N
C
C
TWK-40::tagRFP::ZF
D
A
P
V
AVB
AVA
AVA soma
axon
DVA
PM-GPI
TWK-40::RFP
r = 0.69
D
(i)
+80 mV
-80 mV
Δ 20 mV
400 pA
200 ms
empty vector
TWK-40(WT)
TWK-40(gf)
TWK-40(gf), low [K]i+
(ii)
empty vector
TWK-40(WT)
***
I (pA)
150
75
-75
-80
-40
40
80
V (mV)
(iii)
TWK-40(WT)
TWK-40(gf)
TWK-40(gf)low [K+]i
***
***
I (pA)
600
300
-300
-80
-40
40
80
V (mV)
E
+90 mV
-60 mV
400ms
Current (pA)
200
100
0
-100
*
**
(n=5)
(n=8)
(n=7)
(n=7)
wild type
twk-40(lf)
twk-40(lf);
AVA-TWK-40
twk-40(gf)
F
Cumulative Distribution Function
1
0.9
0.8
0.7
0.6
0.5
0.4
0.3
0.2
0.1
0
-45
-40
-35
-30
-25
-20
-15
-10
-5
0
Membrane Voltage (mV)
wild type
twk-40(lf)
twk-40(lf);
AVA-rescue
twk-40(gf)

Figure 1. TWK-40, K2P, regulates AVA's membrane potential and neuronal excitability.

A. Illustration of sodium leak and potassium leak channels maintaining a negative membrane potential of a neuron.

B. Illustration of the predicted topological structure of TWK-40 (isoform b) with positions of each genetic mutation. LF: *hp834*, null, a 7bp exon deletion that leads to a truncation after TM1. GF: *bln336* (L181N), a pan-K2P activating mutation that promotes channel gating of all K2P channels

C. (Upper left panel), Maximum intensity projection of confocal images of anti-tagRFP immunostained endogenous TWK-40::tagRFP proteins. Dashed lines outline the animal. AVA's soma is denoted by a circle. The arrowhead labels processes along the ventral nerve cord. (Upper right panels, up), AVA and AVB soma; (down) DVA soma. Scale bar, 2µm. (Lower panel) TWK-40 localizes to the plasma membrane. single panel confocal images of co-staining of tagRFP and GFP in *twk-40::tagRFP*; pan-neuronal GPI::YFP animals. Pearson's correlation coefficient is shown.

D. (i) Representative step currents were recorded by whole-cell voltage-clamp from HEK293 cells with expression of different vectors. Cells were held at -80 mV with an increment of +10 mV. (ii, iii), I-V curve with the expression of different vectors with 95% CI. Average currents at +80 mV were analyzed (ii), While mild outward currents were recorded from the cells with expression of TWK-40(WT) (n=13) compared to cell with empty vector (n=12), (iii), larger currents were observed in cells expressing TWK-40(GF) (n=10), revealing that TWK-40 constitutes a functional voltage-insensitive outward channel. (iii) Reloading of the intracellular K^+ from 140 mM to 14 mM diminished the outward currents of TWK-40(GF)(n=7).

E. Averaged traces of AVA's leak current in each genotype by whole-cell patching (ramp currents, holding potential is -60 mV). Mean, black trace. Range, grey. Data at -80mV was compared with wild-type animals (n=5). In *twk-40(lf) (hp834)* (n=8) animals, the leak current is reduced and can be restored by AVA-specific TWK-40 expression (n=7). Leak current is increased in *twk-40(gf) (bln336)* (n=7) animals. The numbers of recorded animals are shown.

F. The cumulative distribution function of AVA's membrane potential (injected 0pA current) shows a more depolarized and hyperpolarized membrane potential in *twk-40(lf)* (n=9) and *twk-40(gf)* (n=13) mutants, respectively, compared to wild-type (n=7) animals. AVA-specific TWK-40 expression reduced the depolarized membrane potential of AVA in *twk-40(lf)* mutant background.

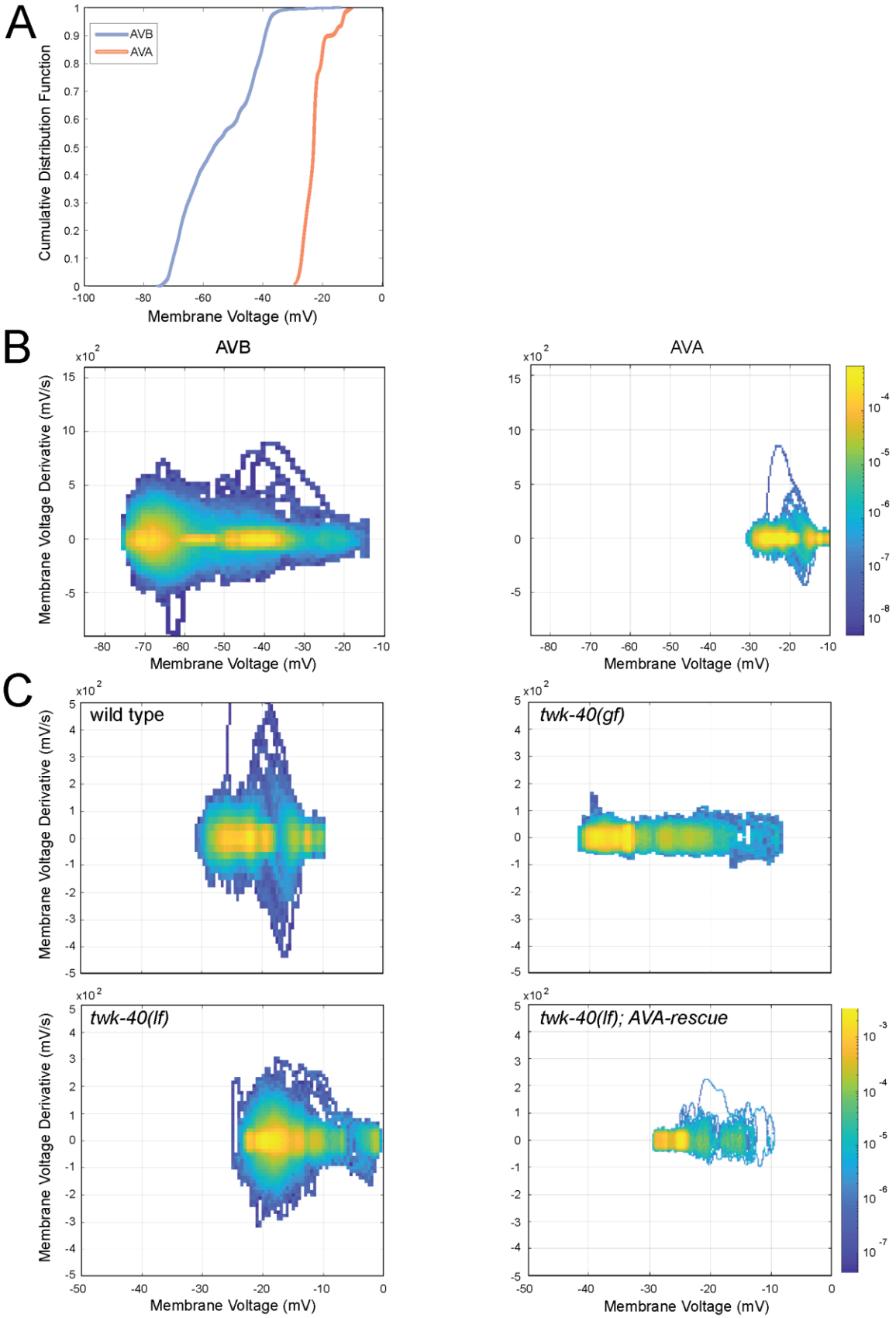
A
AVB
AVA
Cumulative Distribution Function
Membrane Voltage (mV)
B
AVB
AVA
Membrane Voltage Derivative (mV/s)
Membrane Voltage (mV)
C
wild type
twk-40(gf)
twk-40(lf)
twk-40(lf); AVA-rescue
Membrane Voltage Derivative (mV/s)
Membrane Voltage (mV)

Figure 1S1 The unusually depolarized membrane potential of AVA is regulated by TWK-40

A. Cumulative distribution function of AVA (n=7) and AVB's (n=8) membrane potential (injected 0pA current) showing AVA holds a more depolarized membrane potential than AVB.

B. Distribution of membrane potential derivative at each voltage for AVA and AVB.

C. Distribution of membrane potential derivative at each voltage in each genotype showing an increase and decrease of AVA's membrane potential in *twk-40(lf)* (n=9) and *twk-40(gf)* (n=13) mutant, respectively. AVA-specific restoration of TWK-40 decreases the depolarized membrane potential in *twk-40(lf)* mutant background (n=8).

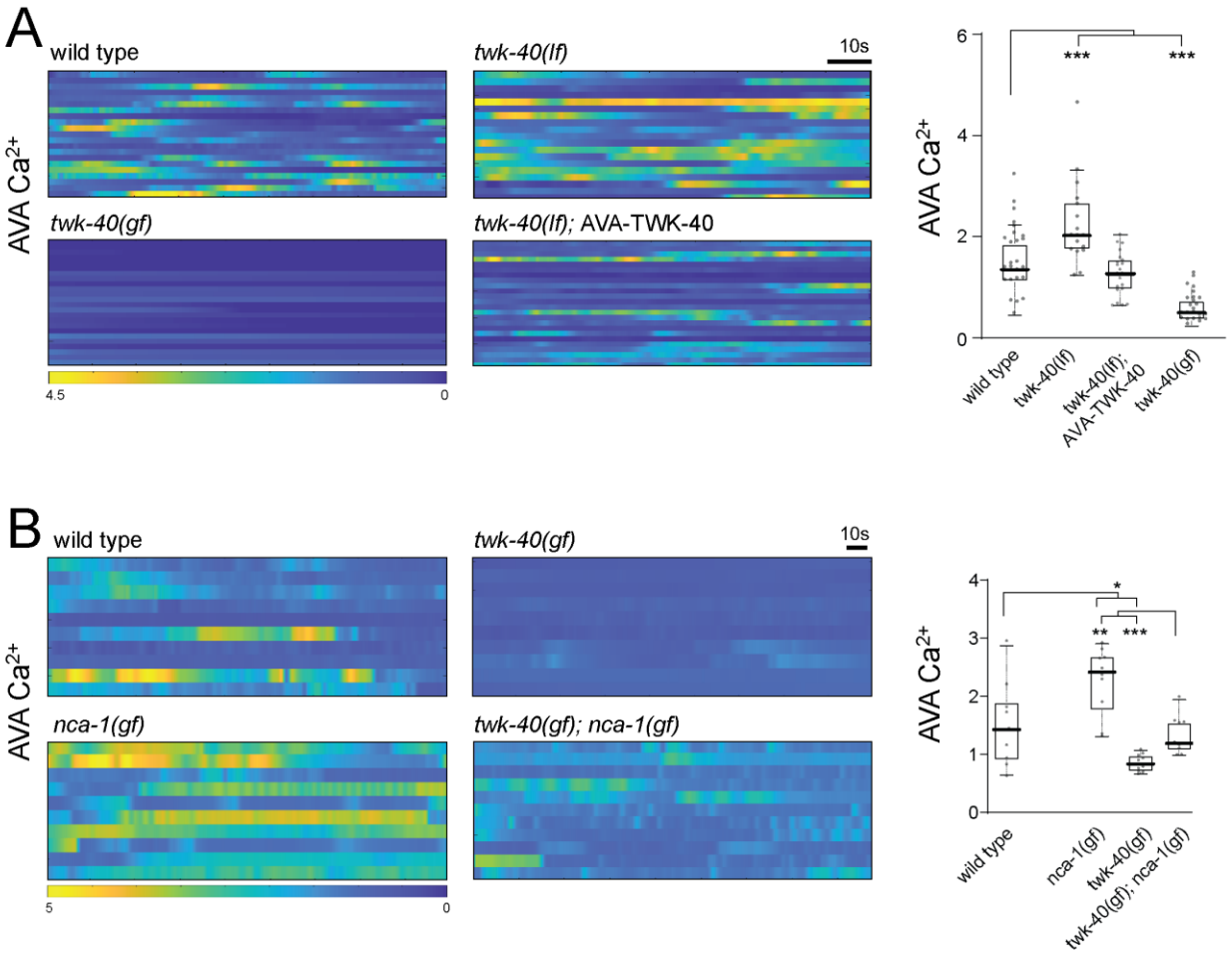

Figure 1S2. TWK-40 together with NCA regulates AVA's excitability

A. (Left panel) Raster plots and (right panel) quantification of overall AVA's activity in freely moving animals (GCaMP/RFP ratio) by genotypes. Each trace represents one animal. *twk-40(lf)* animals (n=17) exhibit increased overall activity of AVA compared to wild-type animals (n=20), which is reduced by the AVA-specific expression of TWK-40 (n=24). *twk-40(gf)* animals (n=24) exhibit reduced overall activities of AVA compared to wild-type animals.

B. (Left panel) Raster plots and (right panel) quantification of AVA soma calcium dynamics in freely moving animals (GCaMP/RFP ratio) of each genotype. Consistent with the behavior[98], *nca-1(gf)* animals (n=9) exhibit increased calcium activity compared to wild-type animals (n=10), partially restoring the activity level in *twk-40(gf); nca-1(gf)* (n=11). Each trace represents one animal.

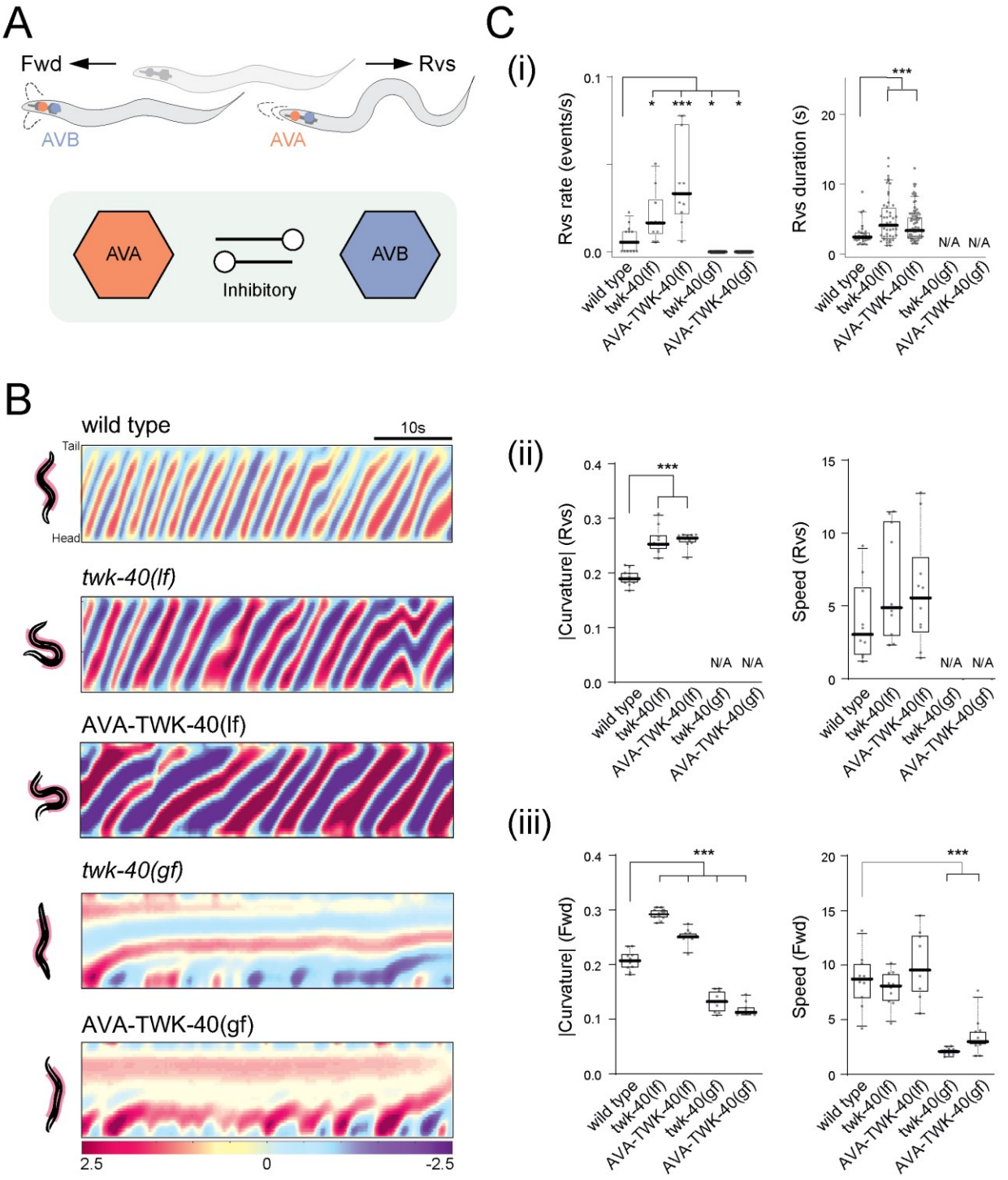
A
Fwd
Rvs
AVB
AVA
AVA
Inhibitory
AVB
B
wild type
10s
Tail
Head
twk-40(lf)
AVA-TWK-40(lf)
twk-40(gf)
AVA-TWK-40(gf)
2.5
0
-2.5
C
(i)
Rvs rate (events/s)
Rvs duration (s)
N/A N/A
(ii)
|Curvature| (Rvs)
Speed (Rvs)
N/A N/A
(iii)
|Curvature| (Fwd)
Speed (Fwd)
wild type
twk-40(lf)
AVA-TWK-40(lf)
twk-40(gf)
AVA-TWK-40(gf)

Figure 2. The premotor interneuron AVA regulates both forward and backward motor movements.

A. The relationship between forward and backward motor patterns has been previously modeled with a reciprocal inhibition between AVA and AVB interneurons.

B. Representative heatmaps of body curvature plot of a freely moving animal of each genotype (the body segment highlighted in magenta is analyzed). *twk-40(lf) (hp834)* and AVA-TWK-40(lf) animals show increased curvature. *twk-40(gf)(bln336)* and AVA-specific TWK-40(gf) animals exhibit slow forward movement with decreased curvature.

C. (i, Left panel) Averaged reversal rate (Rvs) in each genotype. *twk-40(lf)(hp834)* (n=11) and AVA-specific TWK-40(lf) animals (n=11) have increased reversal rates compared to wild-type animals (n=13). No reversal events were detected in *twk-40(gf)(bln336)* (n=11) and AVA-specific TWK-40(gf) (n=11). (i, Right panel) Averaged reversal duration in each genotype. *twk-40(lf)(hp834)* (46 events from 11 animals) and AVA-specific TWK-40(lf) (80 events from 11 animals) exhibit prolonged reversals compared to wild-type animals (30 events from 13 animals). (ii, iii) Averaged curvature (absolute value of radian) and speed during backward and forward movement in each genotype. *twk-40(lf) (hp834)* (n=11) and AVA-TWK-40(lf) (n=11)animals show increased curvature during backward and forward movement compared to wild type animals (n=11). No significant changes in reversal and forward speed were detected in *twk-40(lf)* (n=11) and AVA-specific TWK-40(lf) animals (n=11) compared to wild-type animals (n=11). *twk-40(gf, bln336)* (n=11) and AVA-specific TWK-40(gf) (n=12) exhibit decreased curvature and speed during the forward state. N/A: no events detected.

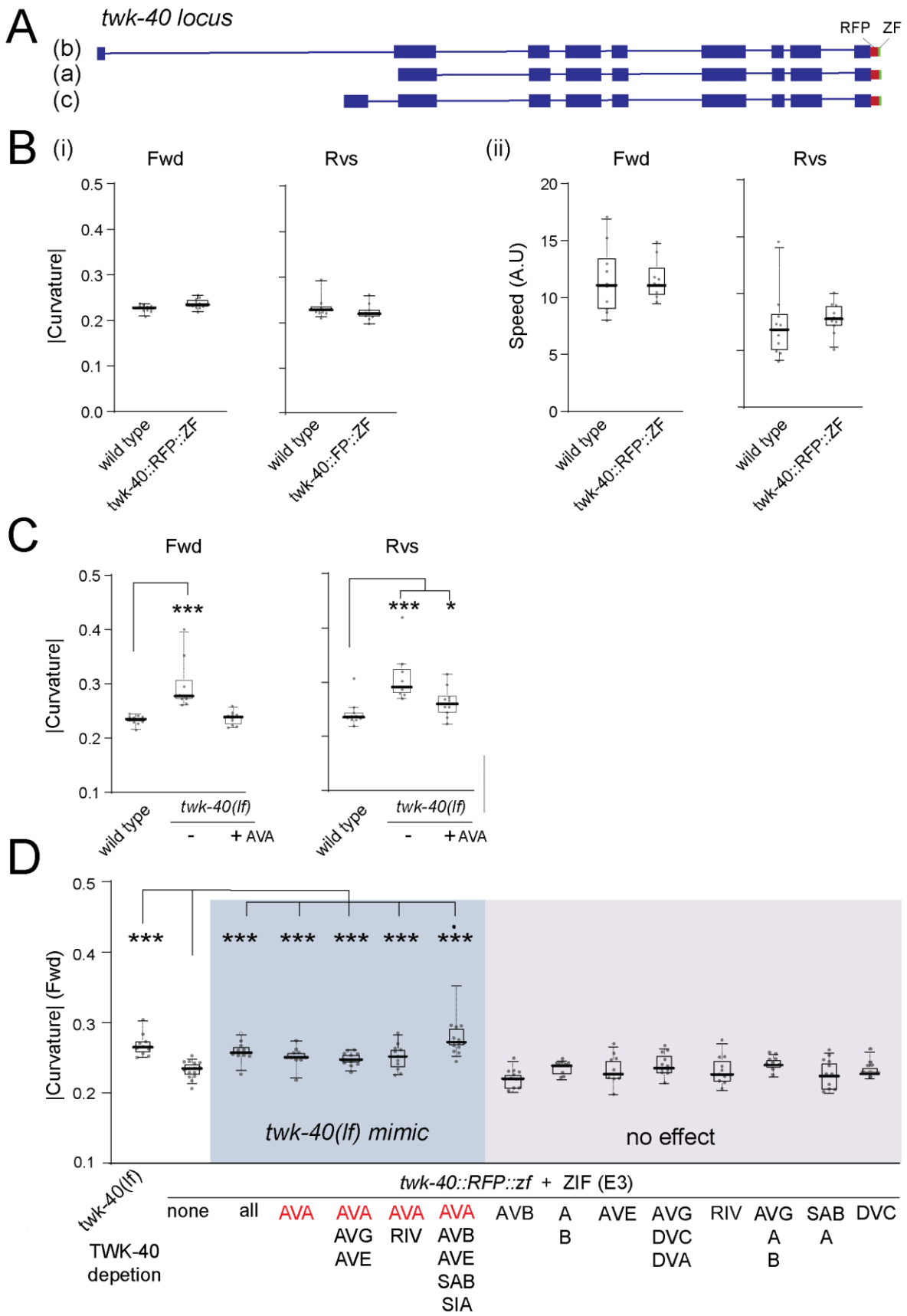
A
twk-40 locus
RFP
ZF
(b)
(a)
(c)
B
(i)
Fwd
Rvs
|Curvature|
wild type
twk-40::RFP::ZF
twk-40::FP::ZF
(ii)
Speed (A.U)
C
***
*
twk-40(lf)
- + AVA
D
|Curvature| (Fwd)
twk-40(lf) mimic
no effect
twk-40::RFP::zf + ZIF (E3)
none
all
AVA
AVA AVG AVE
AVA RIV
AVA AVB AVE SAB SIA
AVB
A B
AVE
AVG DVC DVA
RIV
AVG A B
SAB A
DVC
TWK-40 depetion

Figure 2S1. TWK-40 mainly functions through AVA to regulate curvature during forward movement

A. Predicted gene structures of *twk-40* (isoform a, b, and c). Blue boxes denote exons. Lines denote introns. Red and green boxes denote the insertion of tagRFP and ZF domain at the C-terminus of TWK-40.

B. Averaged curvature (absolute value of radian, i) and speed (ii) in wild-type (n=11) and *bln282 (twk-40::tagRFP::ZF)* animals (n=11). No significant differences were observed in *bln282* animals.

C. Averaged curvature during forward and backward movement in each genotype. AVA-specific TWK-40 expression in *twk-40(lf, hp834)* (n=11) restores its curvature to wild-type level during forward and backward movement compared to wild-type (n=11) and *twk-40(lf) animals* (n=10). "-" denotes absence of a transgene that restored TWK-40 expression in AVA. "+" denotes the presence of a transgene that restored TWK-40 expression in AVA.

D. Averaged curvature (absolute value of radian) during forward movement in *twk-40(lf)*, *bln282*, and animals upon cell-specific depletion of TWK-40. Animals exhibit increased forward curvature only when ZIF-1 is expressed in AVA.

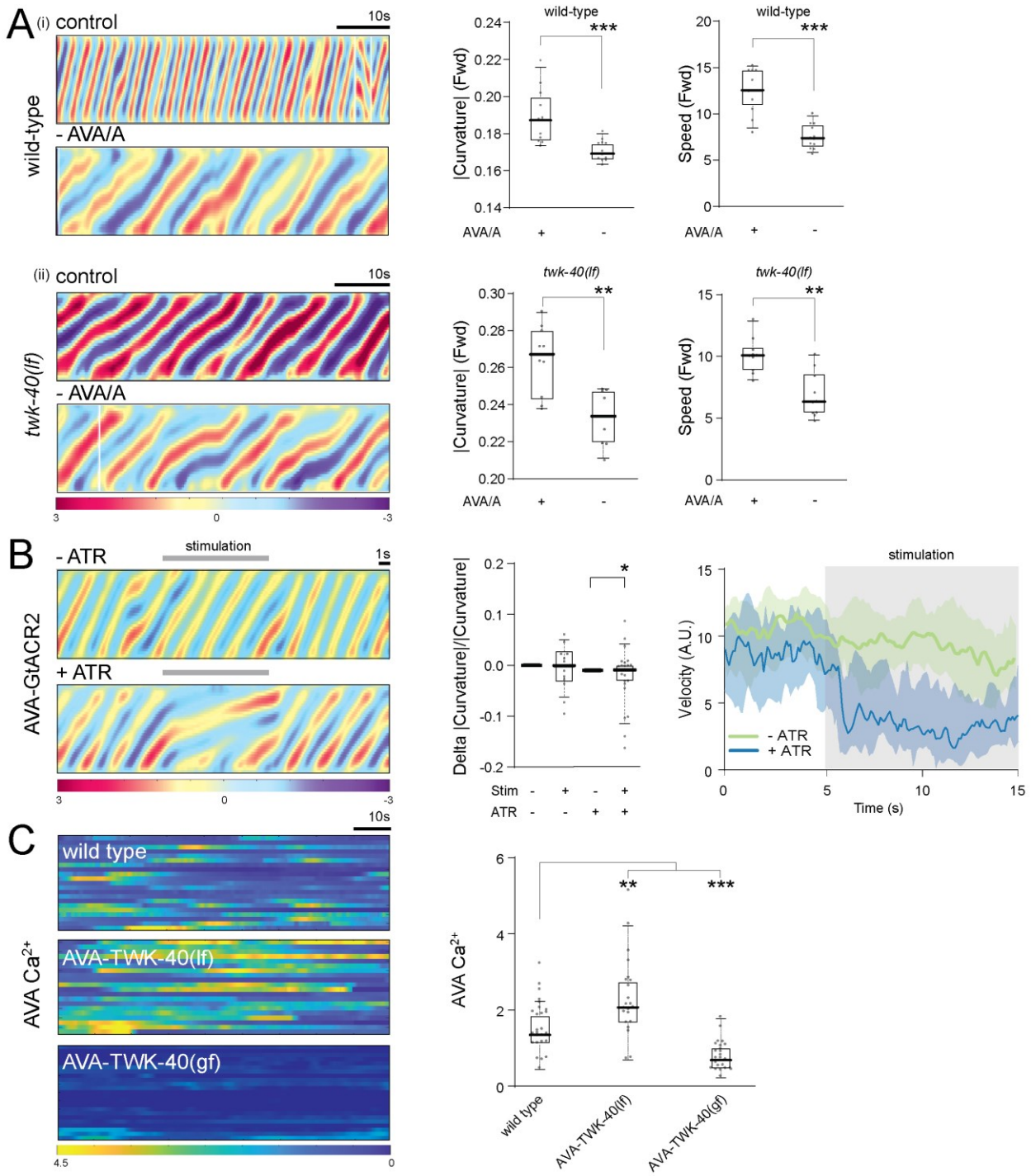
A
(i) control
10s
wild-type
- AVA/A
wild-type
***
|Curvature| (Fwd)
0.24
0.22
0.20
0.18
0.16
0.14
AVA/A
+
-
wild-type
***
Speed (Fwd)
20
15
10
5
0
AVA/A
+
-
(ii) control
10s
twk-40(lf)
- AVA/A
3
0
-3
twk-40(lf)
**
|Curvature| (Fwd)
0.30
0.28
0.26
0.24
0.22
0.20
AVA/A
+
-
twk-40(lf)
**
Speed (Fwd)
15
10
5
0
AVA/A
+
-
B
- ATR
stimulation
1s
AVA-GtACR2
+ ATR
3
0
-3
*
Delta |Curvature|/|Curvature|
0.2
0.1
0.0
-0.1
-0.2
Stim - + - +
ATR - - + +
stimulation
Velocity (A.U.)
15
10
5
0
- ATR
+ ATR
0
5
10
15
Time (s)
C
10s
wild type
AVA-TWK-40(lf)
AVA-TWK-40(gf)
AVA Ca2+
4.5
0
**
***
AVA Ca2+
6
4
2
0
wild type
AVA-TWK-40(lf)
AVA-TWK-40(gf)

Figure 2S2. AVA maintains the forward motor movement.

A. Ablation of AVA/A reduces forward curvature and speed. Representative heatmaps of curvature (eft panels), quantification of averaged curvature ((absolute value of radian, middle panels), and speed (right panels) with AVA/A ablation in wild-type (i, control) (n=13) and *twk-40(lf)* mutants (ii) (n=11) compared to wild-type (n=13) and *twk-40(lf)* (n=11).

B. (Left panel) Representative heatmaps of curvature and quantification of curvature changes (absolute value of radian) and velocity in control (-ATR) (n=28) and stimulated (+ATR) AVA-specific GtACR2 animals (n=25), showing a reduced forward curvature and velocity during stimulation. Shaded bars denote mean and SD.

C. (Left panel) Raster plots and (right panel) quantification of an overall AVA's activity in freely moving animals (GCaMP/RFP ratio) by genotypes. Each trace represents one animal. AVA-specific TWK-40(*lf*) (n=23) and AVA-specific TWK-40(*gf*) animals (n=27) exhibit increased and decreased overall activities of AVA, respectively, compared to wild-type animals (n=23).

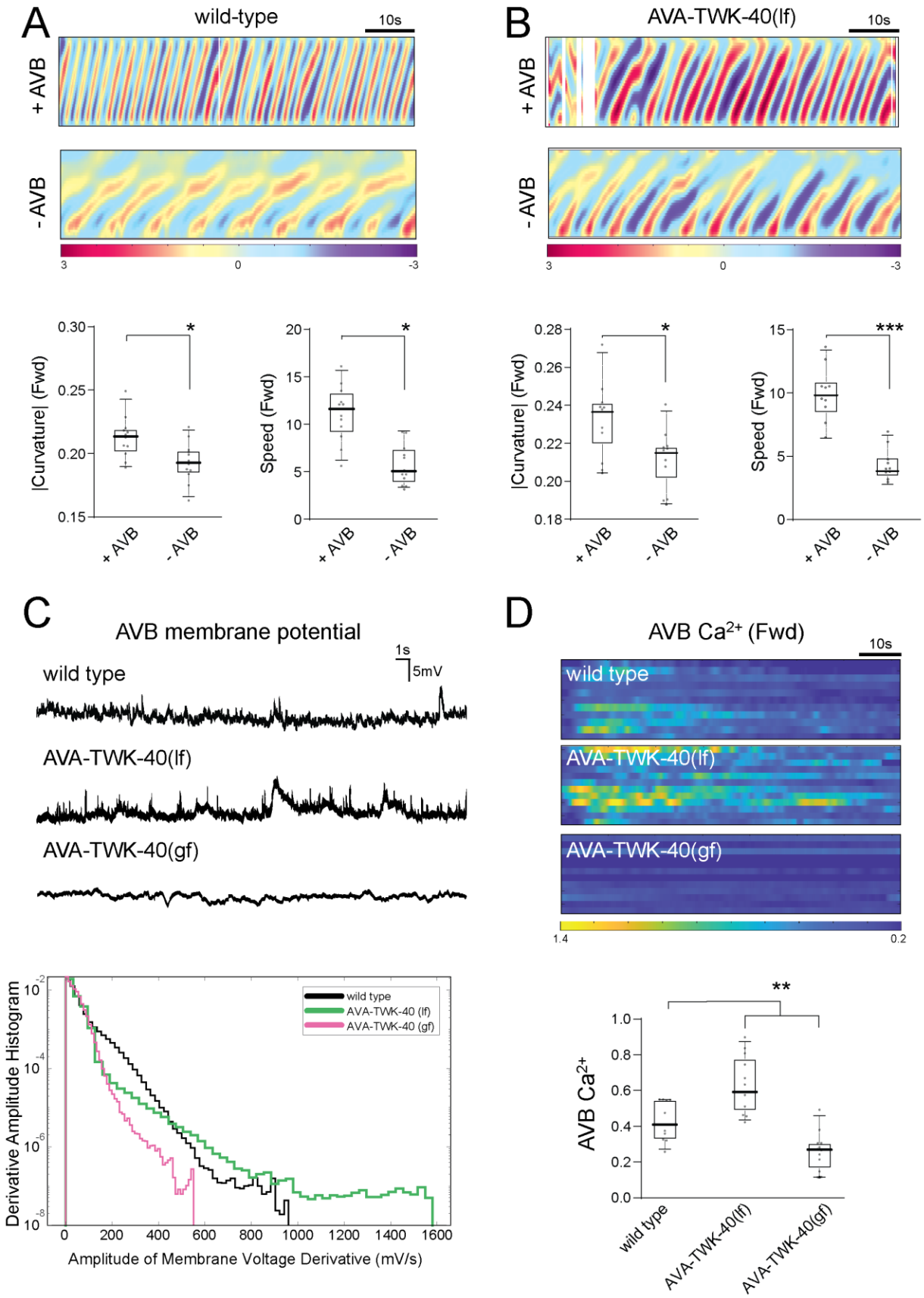
A
wild-type
10s
+ AVB
- AVB
3
0
-3
|Curvature| (Fwd)
Speed (Fwd)
+ AVB
- AVB
B
AVA-TWK-40(lf)
C
AVB membrane potential
1s
5mV
wild type
AVA-TWK-40(lf)
AVA-TWK-40(gf)
D
AVB Ca2+ (Fwd)
1.4
0.2
Derivative Amplitude Histogram
Amplitude of Membrane Voltage Derivative (mV/s)
AVB Ca2+

Figure 3. AVA's activity positively regulates AVB's activity

A. Ablation of AVB leads to significantly reduced forward curvature and speed. (Upper panel) Representative heatmaps of body curvature of control (LED non-treated) (n=13) and AVB ablated (LED treated) animals (n=13). (Lower panel) Averaged curvature (absolute value of radian) and speed during forward movement in each genotype.

B. Ablation of AVB leads to significantly reduced curvature and speed in AVA-specific TWK-40(*lf*) animals. (Upper panel) Representative heatmaps of body curvature of control (LED non-treated) (n=11) and AVB ablated (LED-treated) animals (n=11) in AVA-specific TWK-40(*lf*) background. (Lower panel) Averaged curvature (absolute value of radian) and speed during forward movement in each genotype as in the left panel.

C. (Upper panel), representative traces of membrane potentials of AVB in each genotype upon injection of 0pA current. (Lower panel) Quantification of AVB's membrane potential changes when manipulation of AVA activity, showing that AVB has increased and decreased dynamics in AVA-specific TWK-40(*lf*) (n=7) and AVA-specific TWK-40(*lf*) (n=8) animals, respectively, compared to wild type (n=8).

D. Raster plot and quantification of AVB calcium activity during forward movement, represented by the GCaMP/RFP ratio in freely moving wild-type (n=12), AVA-specific TWK-40(*lf*) (n=14), and AVA-specific TWK-40(*gf*) animals (n=13). Each trace represents one animal. AVB exhibits increased and decreased activities in AVA-TWK-40(*lf*) and AVA-specific TWK-40(*gf*) animals during forward movement, respectively compared to wild-type animals (control).

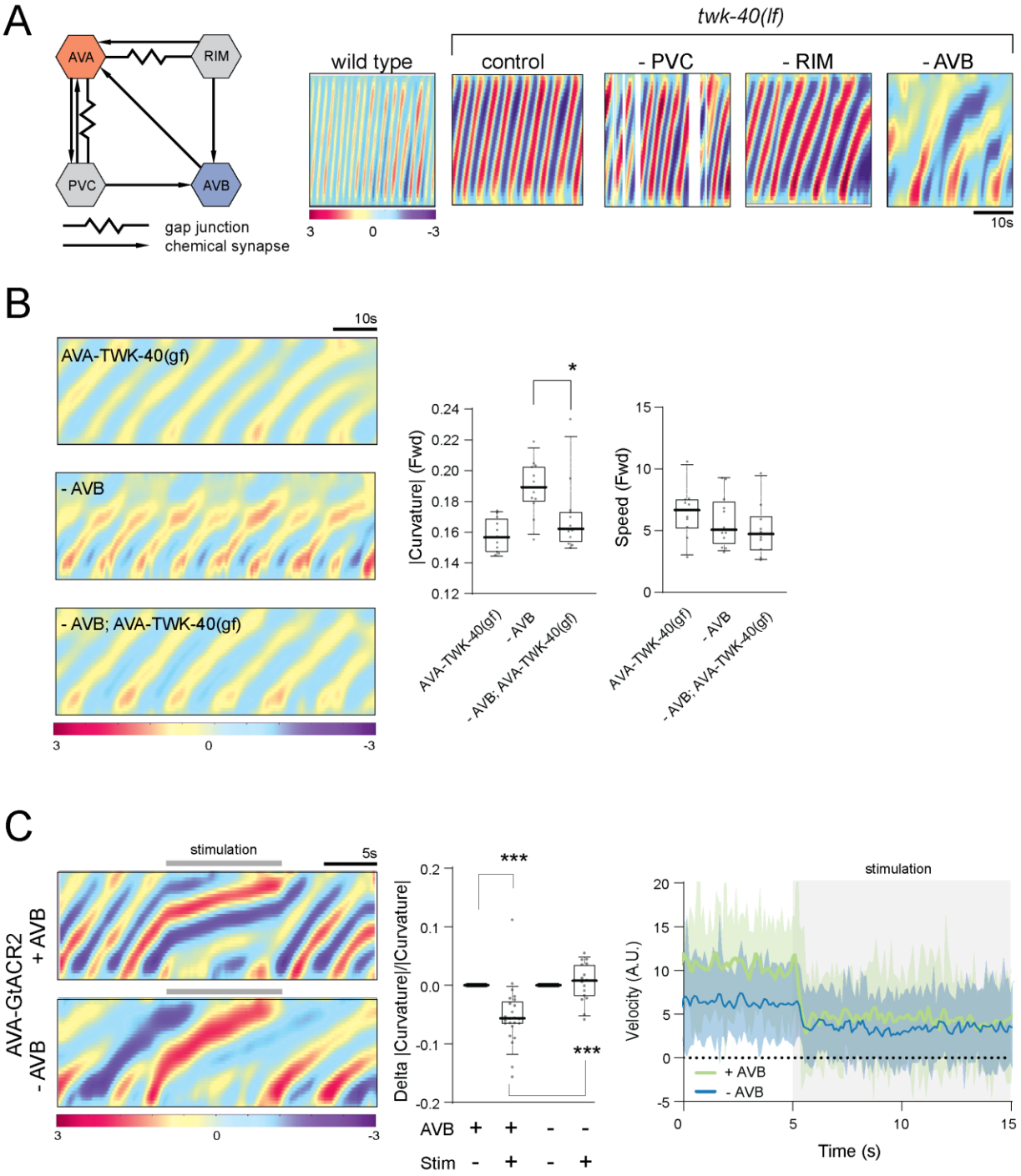
A
AVA
RIM
PVC
AVB
gap junction
chemical synapse
twk-40(lf)
wild type
control
- PVC
- RIM
- AVB
3
0
-3
10s
B
10s
AVA-TWK-40(gf)
- AVB
- AVB; AVA-TWK-40(gf)
3
0
-3
*
|Curvature| (Fwd)
0.24
0.22
0.20
0.18
0.16
0.14
0.12
Speed (Fwd)
15
10
5
0
AVA-TWK-40(gf)
- AVB
- AVB; AVA-TWK-40(gf)
C
stimulation
5s
AVA-GtACR2
+ AVB
- AVB
3
0
-3
***
Delta |Curvature|/|Curvature|
0.2
0.1
0.0
-0.1
-0.2
AVB + + - -
Stim - + - +
stimulation
Velocity (A.U.)
20
15
10
5
0
-5
+ AVB
- AVB
0
5
10
15
Time (s)

Figure 3S1.The effect on forward locomotion when silencing AVA's activity requires AVB

A. (Left panel) Anatomic connectivity between AVA and AVB. (Right panel) Representative heatmaps of curvature of miniSOG ablation of AVB, PVC, or RIM (-) in *twk-40(lf)* mutant animals, showing only ablation of AVB attenuates the increased curvature in *twk-40(lf)* animals.

B. (Left panel) Representative heatmaps of curvature. (Middle panel) Averaged forward curvature (absolute value of radian) in AVA-TWK-40(*gf*) (n=11), control (-AVB, wild-type background) (n=13), and AVA-TWK-40(*gf*) (-AVB) animals (n=11). There is no significant difference between the groups. (Right panel) Averaged d speed during forward locomotion. There is no significant change in forward speed. Forward curvature is mildly but significantly decreased in AVA-TWK-40(*gf*) (-AVB) animals versus control (-AVB) animals, but not significantly changed versus AVA-TWK-40(*gf*) animals.

C. (Left panel) representative heatmaps of body curvature of control (+AVB) (n=25) and AVB ablated (-AVB) animals (n=17) upon weak stimulation in an AVA-Specific GtACR2 expressing background. (Middle and right panel) Velocity and curvature (absolute value of radian) changes in each genotype. Ablation of AVB partially abolished the effect of AVA-specific GtACR2 activation on forward curvature and velocity. Shaded bars denote median and 95% CI.

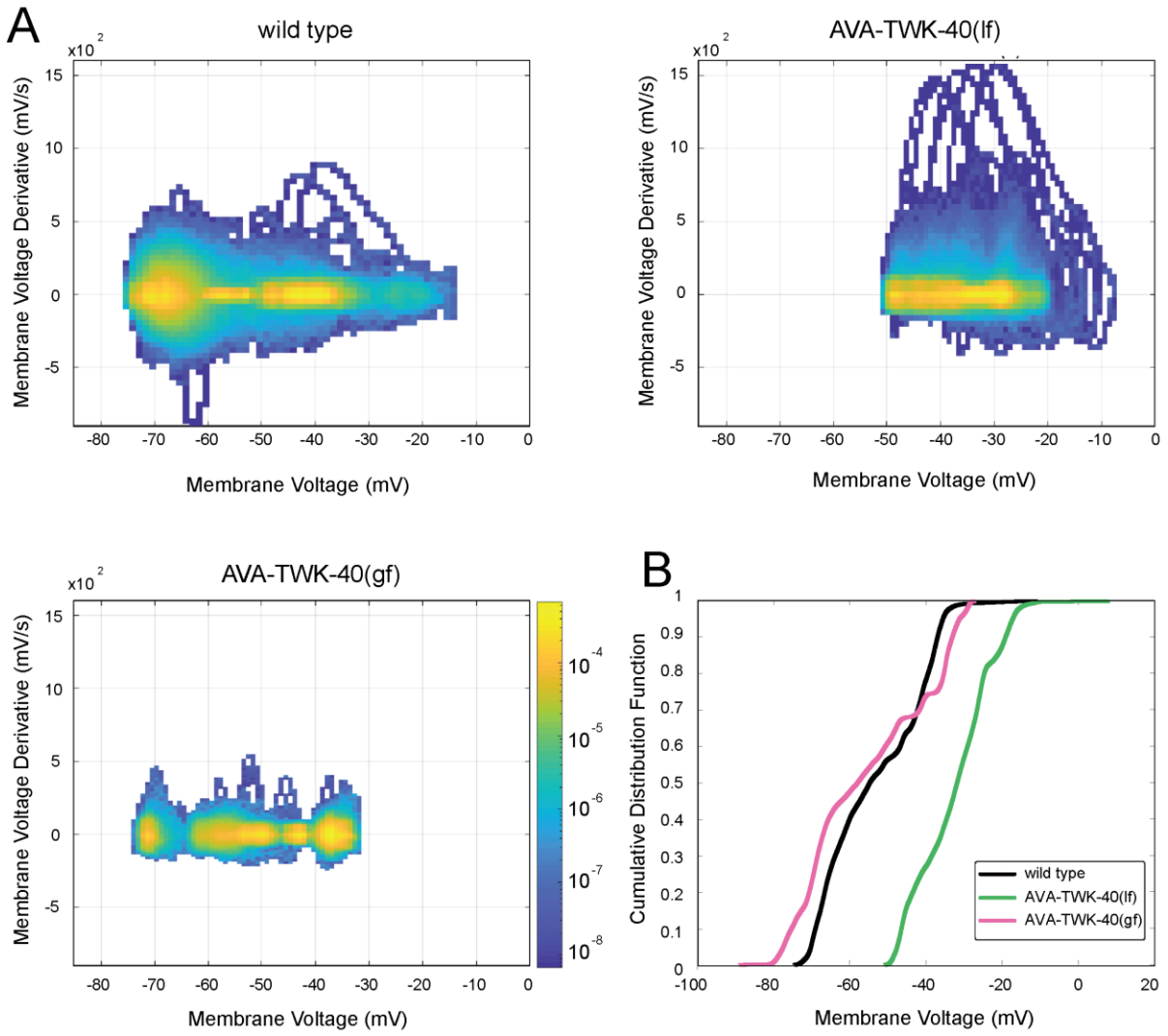

Figure 3S2. Manipulation of AVA's membrane potential has a positive effect on AVB's membrane potential

A. Distribution of membrane potential derivative at a given voltage in each genotype showing an increase and decrease of AVB's membrane potential changes in AVA-TWK-40(*lf*) (n=7) and AVA-TWK-40(*gf*) (n=7) mutant, respectively, compared to wild-type animals (control).

B. Cumulative distribution function of AVB's membrane potential (0pA injected current) showing a more depolarized and hyperpolarized membrane potential in AVA-*twk-40(lf)* and AVA-*twk-40(gf)* mutants, respectively, compared to wild-type animals (control).

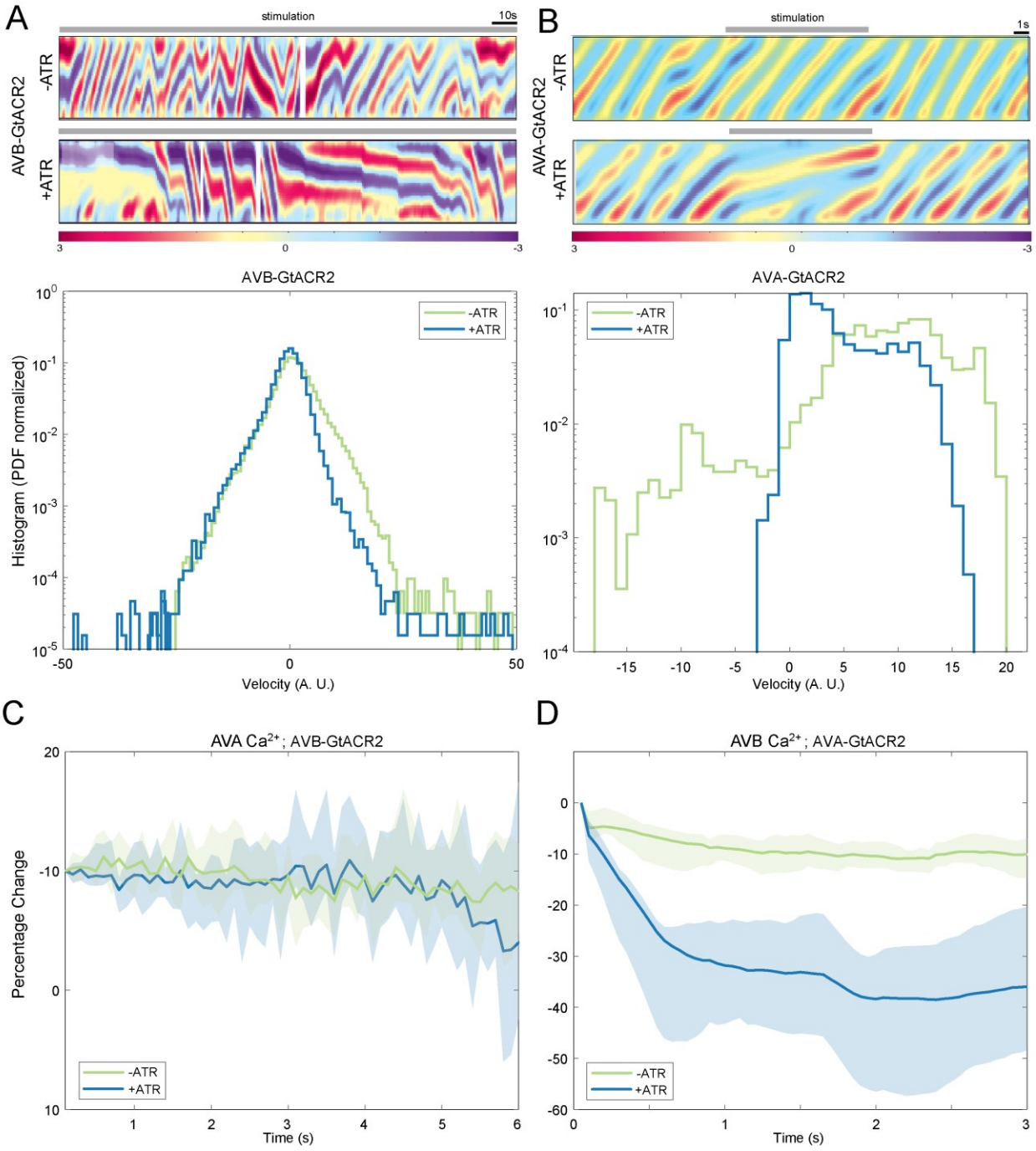
A
stimulation
10s
AVB-GtACR2
-ATR
+ATR
3
0
-3
B
stimulation
1s
AVA-GtACR2
-ATR
+ATR
3
0
-3
AVB-GtACR2
Histogram (PDF normalized)
Velocity (A. U.)
-ATR
+ATR
AVA-GtACR2
Velocity (A. U.)
-ATR
+ATR
C
AVA Ca2+ ; AVB-GtACR2
Percentage Change
Time (s)
-ATR
+ATR
D
AVB Ca2+ ; AVA-GtACR2
Time (s)
-ATR
+ATR

Figure 4. AVA and AVB relationship is largely uni-directional.

A. (Upper panels) Representative heatmaps of curvature. (Lower panel) Normalized probability density function in AVB-GtACR2 animals during blue light stimulation. Silencing AVB (AVB-GtACR2 (ATR+), n=11) leads to a decrease in forward speed without affecting backward movement compared to (-ATR) animals (n=5).

B. (Upper panel) Representative heatmaps of curvature in AVA-GtACR2 (-ATR and +ATR) pre-, during, and post-blue light stimulation. (Lower panel) Normalized probability density function in AVA-GtACR2 during blue light stimulation. Silencing AVA (AVA-GtACR2 (+ATR), n=28) led to decreased forward speed and abolished backward movement compared to (-ATR) animals (n=25).

C. AVA calcium activity (GCaMP/RFP) in immobilized animals that expressed AVB-GtACR2. Silencing AVB (+ATR) (n=28) does not lead to obvious changes during blue light stimulation compare to (-ATR) animals (n=19).

D. AVB calcium activity (GCaMP/RFP) in immobilized animals that expressed AVA-GtACR2. Silencing AVA led to reduced AVB calcium activity in (+ATR) animals (n=23) during blue light stimulation compare to (-ATR) animals (n=23). Shaded bars indicate 95% confidence interval of the mean (C, D).

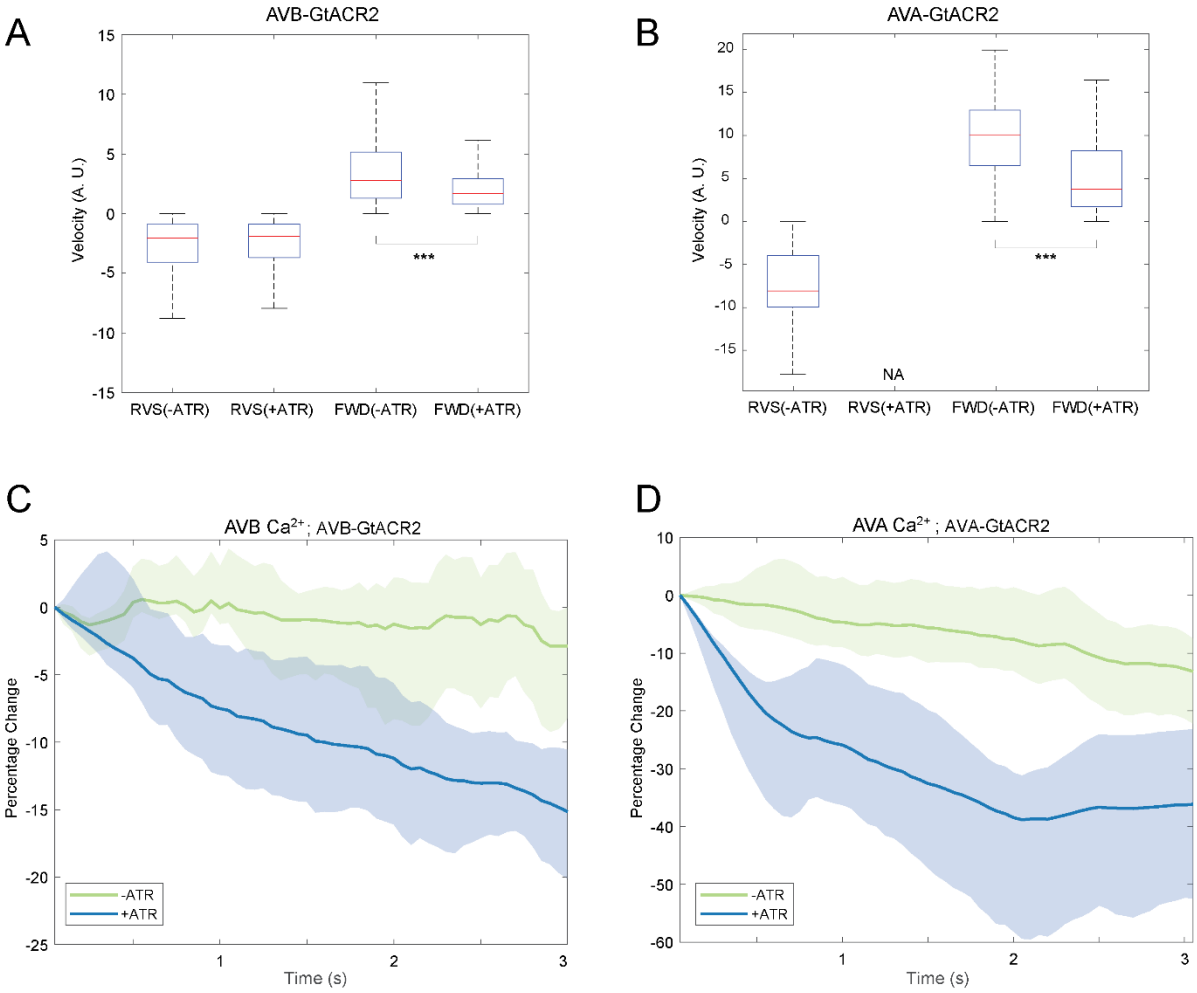
A
AVB-GtACR2
Velocity (A. U.)
15
10
5
0
-5
-10
-15
***
RVS(-ATR)
RVS(+ATR)
FWD(-ATR)
FWD(+ATR)
B
AVA-GtACR2
Velocity (A. U.)
20
15
10
5
0
-5
-10
-15
***
NA
RVS(-ATR)
RVS(+ATR)
FWD(-ATR)
FWD(+ATR)
C
AVB Ca2+; AVB-GtACR2
Percentage Change
5
0
-5
-10
-15
-20
-25
-ATR
+ATR
1
2
3
Time (s)
D
AVA Ca2+ ; AVA-GtACR2
Percentage Change
10
0
-10
-20
-30
-40
-50
-60
-ATR
+ATR
1
2
3
Time (s)

Figure 4S. AVA-AVB relationship is largely unidirectional.

A. Silencing AVB (AVB-GtACR2 (+ATR), n=11) leads to a decrease in forward speed without affecting backward movement compared to (-ATR) animas (n=5).

B. Silencing AVA (AVA-GtACR2 (+ATR), n=28) led to decreased forward speed and abolished backward movement compared to (-ATR) animas (n=25).

C. Silencing AVB (+ATR) (n=28) does not lead to obvious changes during blue light stimulation compared to (-ATR) animas (n=19). AVA calcium activity (GCaMP/RFP) in immobilized animals that expressed AVB-GtACR2.

D. Silencing AVA led to reduced AVB calcium activity in (+ATR) animals (n=23) during blue light stimulation compared to (-ATR) animas (n=23). AVB calcium activity (GCaMP/RFP) in immobilized animals that expressed AVA-GtACR2. Shaded bars indicate 95% confidence interval of the mean (C, D).

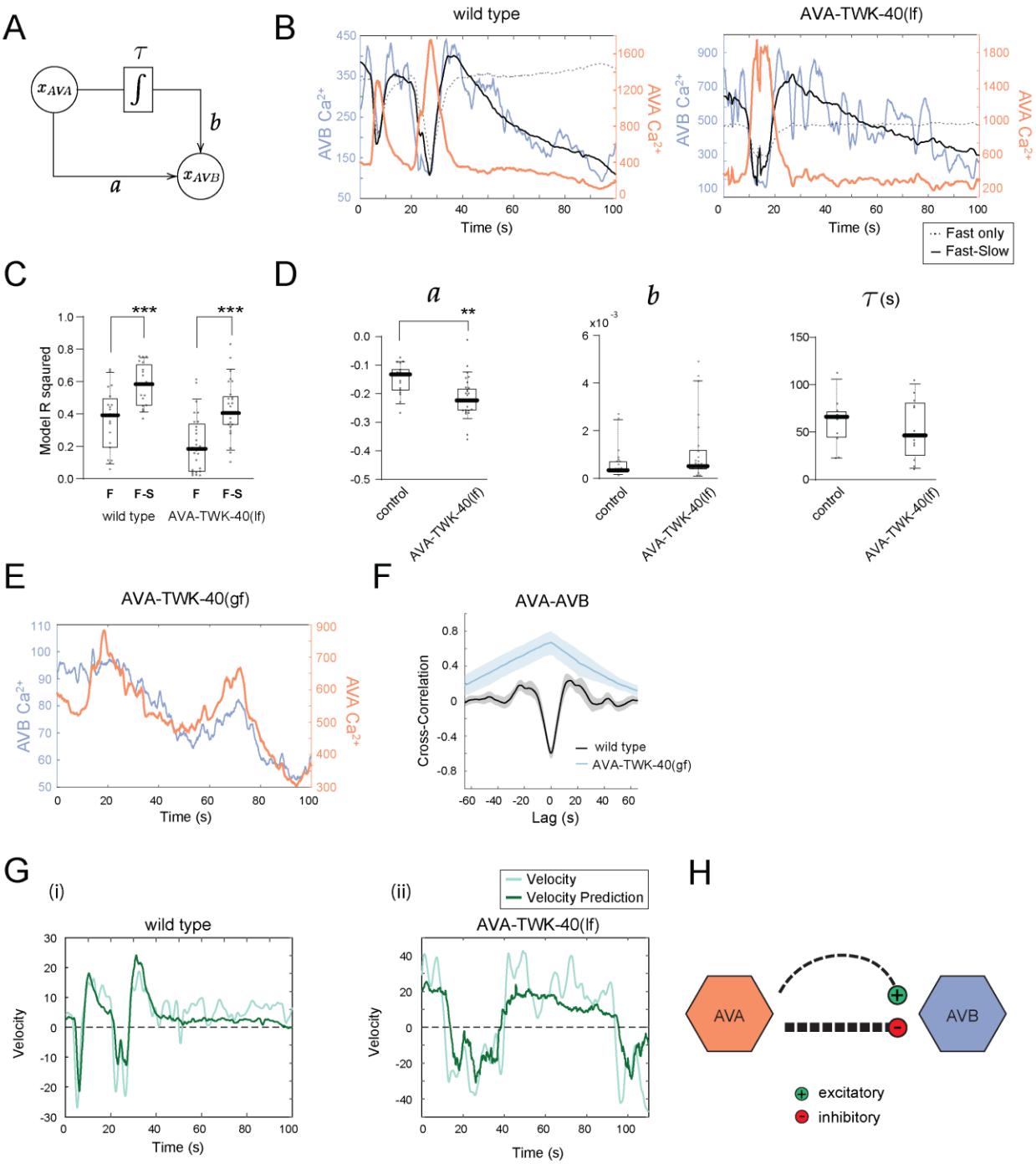
A
x_{AVA}
τ
b
a
x_{AVB}
B
wild type
AVA-TWK-40(lf)
AVB Ca2+
AVA Ca2+
Time (s)
Fast only
Fast-Slow
C
Model R sqaured
***
***
F
F-S
F
F-S
wild type
AVA-TWK-40(lf)
D
a
b
τ (s)
**
x10-3
control
AVA-TWK-40(lf)
E
AVA-TWK-40(gf)
AVB Ca2+
AVA Ca2+
Time (s)
F
AVA-AVB
Cross-Correlation
Lag (s)
wild type
AVA-TWK-40(gf)
G
(i)
wild type
Velocity
Time (s)
(ii)
Velocity
Velocity Prediction
AVA-TWK-40(lf)
Velocity
Time (s)
H
AVA
AVB
excitatory
inhibitory

Figure 5. A two-timescale model captures the AVA-AVB calcium relationship and velocity.

A. AVB activity after a reversal is modeled as a sum of two terms dependent on AVA's activity. A fast negative copy with a proportionality constant a and a slow positive copy integrated with a timescale τ and proportionality constant b

B. (Left panel) Example calcium activity traces show that in the wild-type animal (control), the fast-slow model is a better fit for AVB's post-reversal activity compared to a model without the slow timescale. (Right panel) Example calcium traces show that the fast-slow model also explains AVB's activity in AVA-specific-TWK-40(*lf*).

C. Model R-squared values comparing the performance of the fast-slow model with the fast models in wild-type (control) and AVA-specific-40(*lf*) animals. In both cases, removing the slow timescale decreases model performance.

D. The estimated values of parameters a, b, and the integration timescale for the slow copy τ (reversal events: n=11 for WT and n=10 for TWK-40(*gf*)).

E. Example calcium traces from AVA-specific-TWK-40(*gf*) mutants. AVA-specific-TWK-40(*gf)* negatively affects AVA's output. The relationship flips and we observe a strong positive correlation between AVA and AVB activities.

F. Cross-correlation between AVA and AVB calcium activity quantifying the relationships between the two neurons. Compared to wild-type (control, n=29), AVA-specific-TWK-40(*gf*) (n=13) animals show a strong positive correlation.

G. The model predicts centroid velocity in freely moving wild-type and AVA-specific *twk-40(lf)* animals with AVA's calcium activity. (sample traces. WT params: $a = -0.51, b = 0.02, \tau = 3.5$s; TWK-40(*gf*) params: $a = -0.38, b = 0.004, \tau = 16.6$s).

H. The two-timescale model of AVA-AVB suggests a fast inhibition and a slow excitation from AVA to AVB.

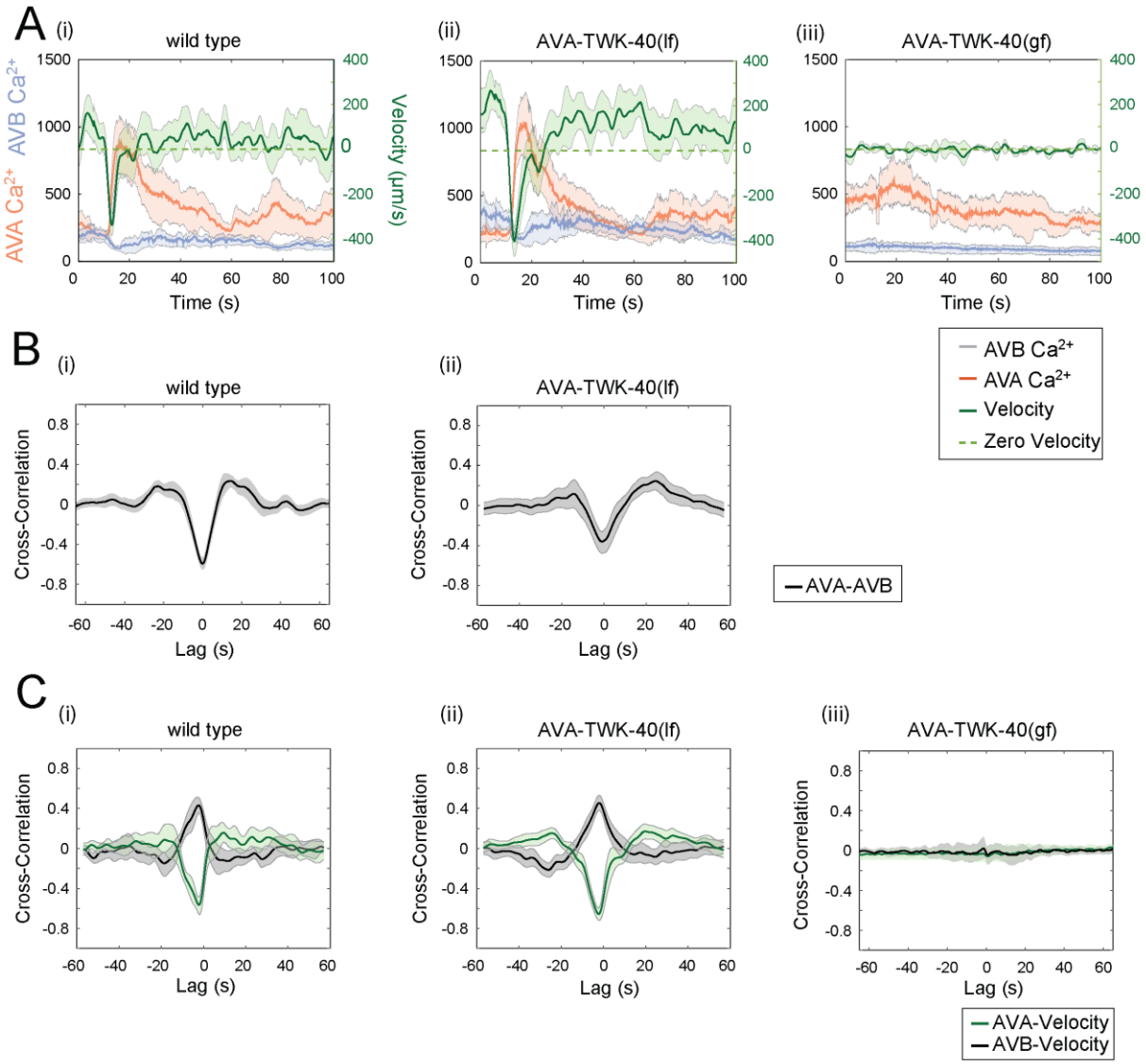
A
(i)
wild type
(ii)
AVA-TWK-40(lf)
(iii)
AVA-TWK-40(gf)
AVA Ca2+
AVB Ca2+
Velocity (µm/s)
Time (s)
B
Cross-Correlation
Lag (s)
AVB Ca2+
AVA Ca2+
Velocity
Zero Velocity
AVA-AVB
C
AVA-Velocity
AVB-Velocity

Figure 5S. A two-timescale model captures the AVA-AVB calcium relationship.

A. Average AVA and AVB calcium activity aligned to the start of an AVA transient for wild-type, AVA-TWK-40(*lf*), and AVA-TWK-40(*gf*) animals respectively. Velocity is plotted in green on the right y-axis (WT: n=19; AVA-TWK-40*(lf*): n=27; AVA-TWK-40(*gf*): n=4). Shaded bars indicate 95% confidence interval of the mean.

B. Averaged cross-correlations between AVA-AVB activity for the data used in panel A

C. The two-timescale model could also be used to predict the animal's centroid velocity from AVA activity alone. Sample traces from the three strains where the model is valid are shown.

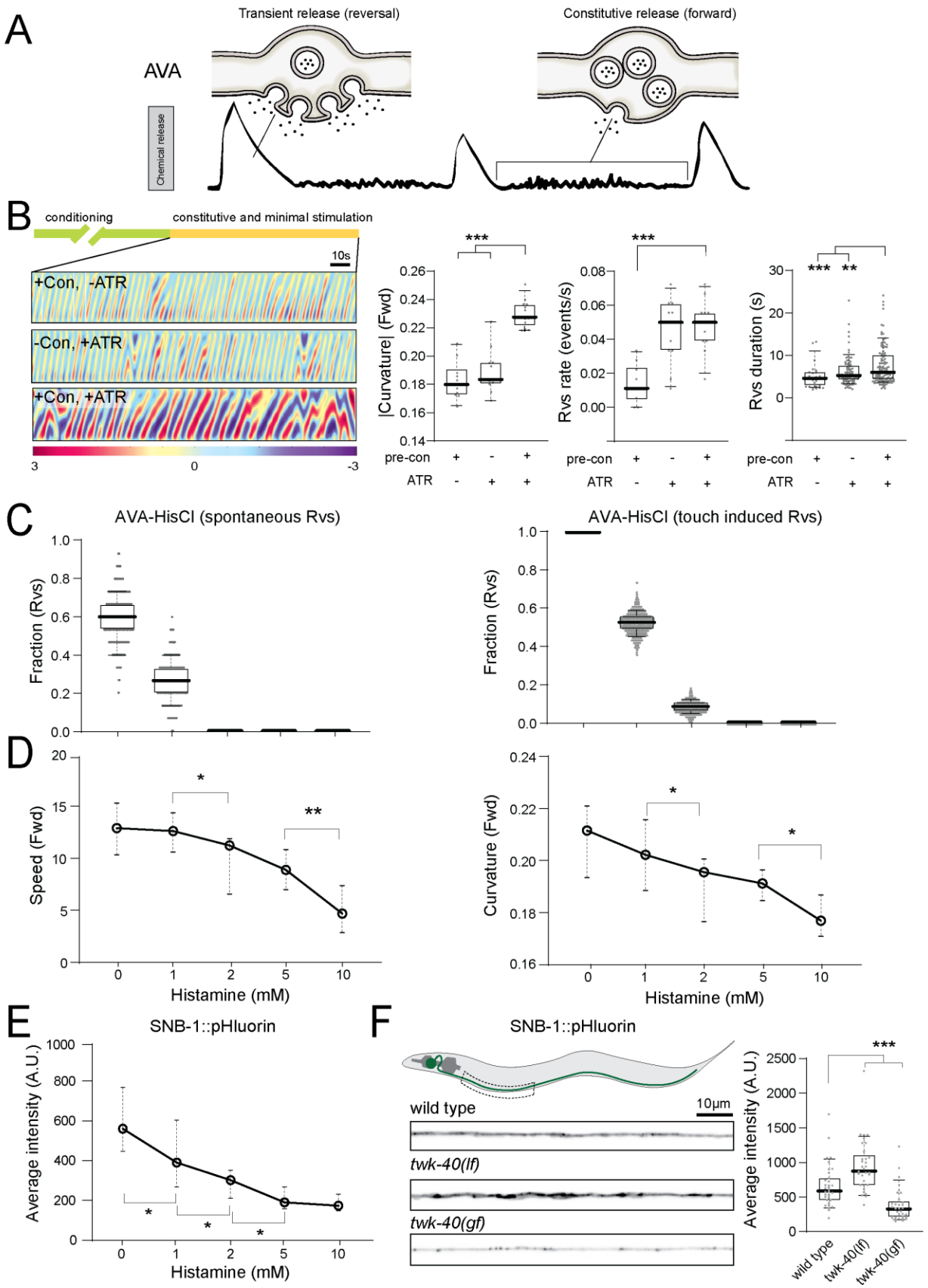
A
AVA
Chemical release
Transient release (reversal)
Constitutive release (forward)
B
conditioning
constitutive and minimal stimulation
10s
+Con, -ATR
-Con, +ATR
+Con, +ATR
3
0
-3
|Curvature| (Fwd)
Rvs rate (events/s)
Rvs duration (s)
pre-con
ATR
C
AVA-HisCl (spontaneous Rvs)
AVA-HisCl (touch induced Rvs)
Fraction (Rvs)
D
Speed (Fwd)
Curvature (Fwd)
Histamine (mM)
E
SNB-1::pHluorin
Average intensity (A.U.)
Histamine (mM)
F
SNB-1::pHluorin
wild type
10µm
twk-40(lf)
twk-40(gf)
Average intensity (A.U.)
wild type
twk-40(lf)
twk-40(gf)

Figure 6. AVA regulates forward movement mainly through chemical synaptic transmission.

A. Illustration of the transient and constitutive chemical release of AVA for the regulation of forward and backward locomotion.

B. (Left panel) Representative heatmaps of curvature of AVA-specific Chrimson animals. With green LED light pre-exposure but without ATR treatment (+Con-exp, -ATR, control, n=10), with ATR treatment but without green LED light pre-exposure (-Con-exp, +ATR, n=10), and with ATR treatment and green LED light pre-exposure ((+Con-exp, +ATR, n=14). (Right panels) Averaged forward bending curvature (absolute value of radian), reversal rate, and reversal duration in each condition. Animals with weak stimulation only exhibit an increased reversal rate. Animals with constitutive, minimal stimulation exhibit increased reversal rate and increased curvature during forward movement.

C. Exposure to 2 mM histamine blocks spontaneous reversal. Fraction of reversals (Rvs) during spontaneous movement animals (n=15) at different histamine concentrations (left panel). Touch-induced (evoked) reversal is strongly reduced in the presence of 2 mM histamine. Fraction of reversal during evoked reversal (n=80 touch events) at different histamine concentrations (right panel).

D. (Left panel) forward speed and (Right panel) forward curvature (absolute value of radian) at different histamine concentrations, showing a gradual reduction in forward speed and curvature upon exposure to increasing histamine levels (each concentration=15).

E. Average AVA-SNB-1::pHluorin fluorescent signals of ventral cord at different histamine concentrations, showing a gradual increase upon increasing histamine concentration (0nM=30, 1 nM =29, 2 nM =30, 5 nM =31, 10 nM =28).

F. Illustration, representative confocal image and quantification of AVA-SNB-1::pHluorin fluorescent intensity in wild-type (n=34), *twk-40(lf)* (n=32), and *twk-40(gf)* (n=32) mutants. AVA-SNB-1::pHluorin fluorescence intensity was significantly increased and decreased in *twk-40(lf)* and *twk-40(gf)* mutants, respectively, compared to wild-type.

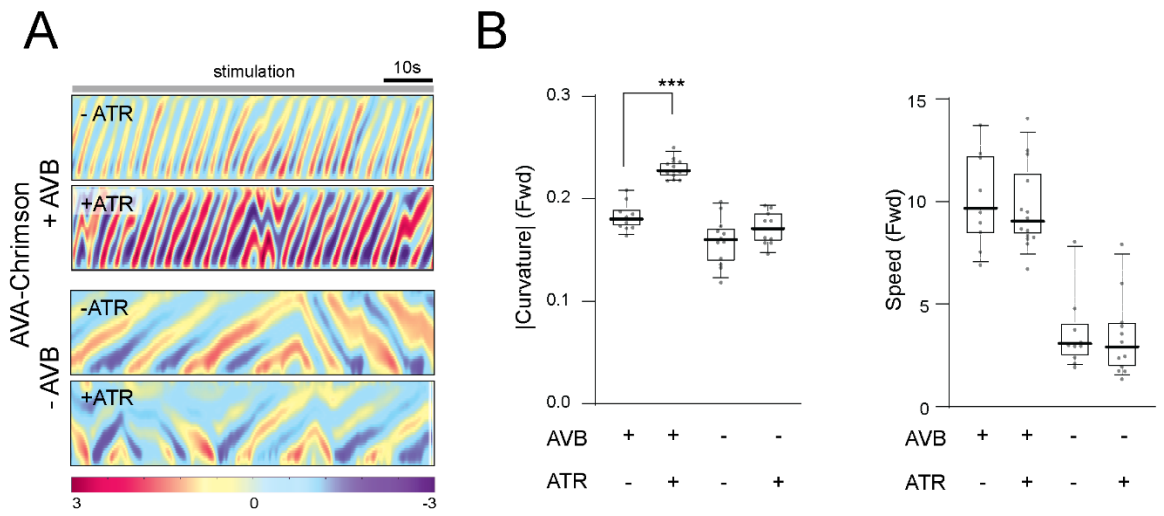

Figure 6S. AVA's constitutive activation of forward locomotion requires AVB

A. Representative heatmaps of curvature of AVA-specific Chrimson-expressing animals under constitutive and minimal activation of AVA with or without AVB.
B. (Right panel) Averaged forward curvature (absolute value of radian) and (right panel) forward speed of AVA-specific Chrimson-expressing animals under constitutive and minimal activation of AVA with or without AVB, showing ablation of AVB no longer induced an increased forward movement by constitutive and minimal activation of AVA (+AVB; -ATR=10, +AVB; +ATR=13, -AVB, -ATR=12, -AVB; +ATR=10).

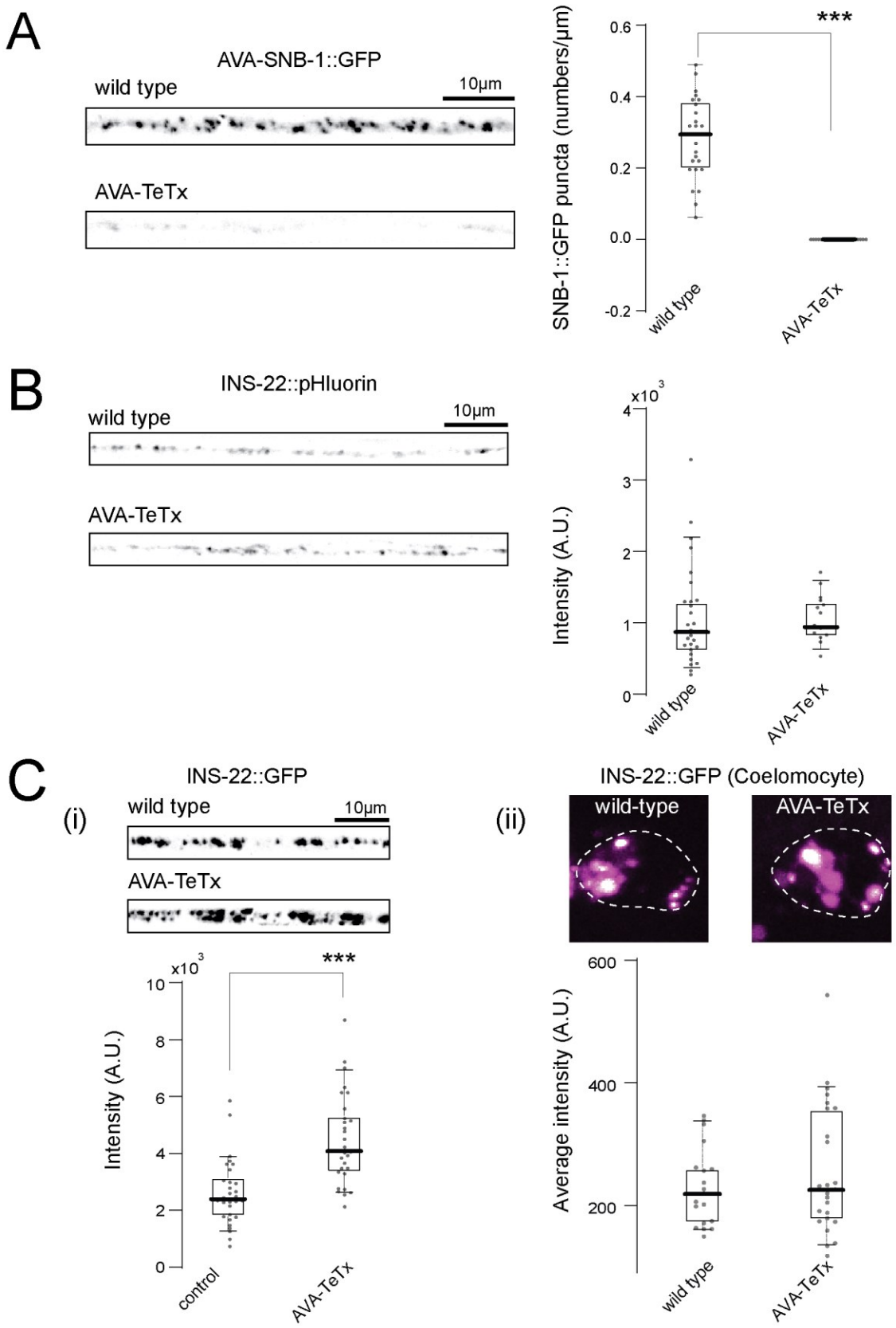
A
AVA-SNB-1::GFP
wild type
10μm
AVA-TeTx
SNB-1::GFP puncta (numbers/μm)
0.6
0.4
0.2
0.0
-0.2
***
wild type
AVA-TeTx
B
INS-22::pHluorin
wild type
10μm
AVA-TeTx
Intensity (A.U.)
x10^3
4
3
2
1
0
wild type
AVA-TeTx
C
(i)
INS-22::GFP
wild type
10μm
AVA-TeTx
Intensity (A.U.)
x10^3
10
8
6
4
2
0
***
control
AVA-TeTx
(ii)
INS-22::GFP (Coelomocyte)
wild-type
AVA-TeTx
Average intensity (A.U.)
600
400
200
wild type
AVA-TeTx

Figure 7. TeTx does not significantly impair neuropeptide secretion from AVA

A. Representative and quantification of SNB-1::GFP from AVA in wild-type, AVA-specific TeTx-expressing animals, showing a lack of SNB-1::GFP puncta in AVA-specific TeTx animals (n=22) compared to wild-type animals (n=25).

B. Maximum intensity projection of a neuropeptide secretion marker (INS-22::PHluorin) in AVA ventral cord processes showing no changes in AVA-specific TeTx-expressing animals. Quantification of averaged PHluorin fluorescence intensity of each puncta shows no significant changes in AVA-specific TeTx animals (n=15) compared to wild-type animals (n=27).

C. (i) Maximum intensity projection of a neuropeptide marker (INS-22::GFP) in AVA ventral cord process. (i), quantification of averaged INS-22::GFP intensity of each puncta, showing an increased fluorescent intensity in AVA-TeTx-expressing animals (n=30) compared to wild-type animals (n=30). (ii) Maximum intensity projection of confocal images of coelomocytes which accumulate secreted neuropeptides in wild-type and AVA-TeTx-expressing animals. (ii) Quantification of average fluorescence intensity of GFP in coelomocytes shows no differences between wild-type (n=20) and TeTx animals (n=26).

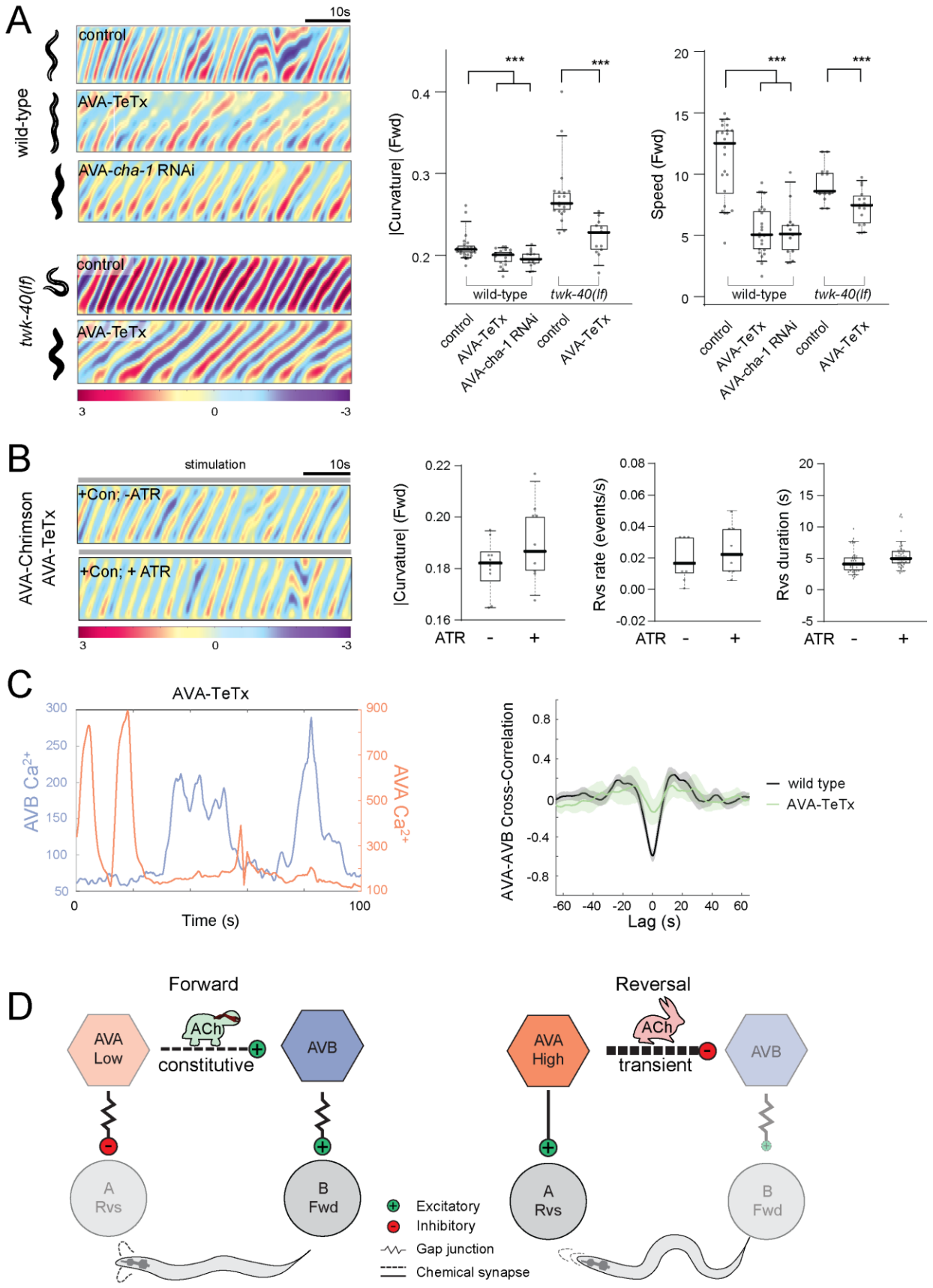
A
10s
control
AVA-TeTx
AVA-cha-1 RNAi
wild-type
control
AVA-TeTx
twk-40(lf)
3
0
-3
|Curvature| (Fwd)
Speed (Fwd)
***
wild-type
twk-40(lf)
control
AVA-TeTx
AVA-cha-1 RNAi
control
AVA-TeTx
B
stimulation
10s
AVA-Chrimson
AVA-TeTx
+Con; -ATR
+Con; + ATR
|Curvature| (Fwd)
Rvs rate (events/s)
Rvs duration (s)
ATR
-
+
C
AVA-TeTx
AVB Ca2+
AVA Ca2+
Time (s)
AVA-AVB Cross-Correlation
Lag (s)
wild type
AVA-TeTx
D
Forward
Reversal
AVA Low
AVB
ACh
constitutive
AVA High
transient
A Rvs
B Fwd
Excitatory
Inhibitory
Gap junction
Chemical synapse

Figure 8. Cholinergic signaling from AVA contributes to bi-direction regulation of the forward motor state

A. Representative heatmaps of the curvature (left panel), averaged curvature (absolute value of radian, middle panel), and speed (right panel) during forward movement in each genotype. Curvature during forward movement and speed are reduced in AVA-specific TeTx in both wild-type (control) and *twk-40(lf)* background animals. AVA-*cha-1* RNAi has a similar effect on the forward movement as AVA-TeTx (WT: control=23, AVA-TeTx=18, AVA-*cha-1* RNAi=14; *twk-40(lf)*: control=20, AVA-TeTx=14).

B. (Left panel) Representative curvature heatmaps upon constitutive, minimal stimulation of animals expressing AVA-specific Chrimson and specific TeTx. (Right panel) Averaged forward curvature (absolute value of radian), forward to backward transition frequency, and reversal duration of AVA-specific Chrimson; specific TeTx animals. No significant changes were observed in all parameters (+Con; -ATR=10, +Con; +ATR=11).

C. (Left panel) Example of AVA and AVB GCaMP in AVA-specific TeTx animals during free movement. (Right panel) Cross-correlation of AVA and AVB activity showing the antiphasic relationship is reduced in AVA-specific TeTx animals (n=10) compared to wild-type (n=19).

D. (Left panel) AVA is a master regulator of spontaneous locomotion. During forward movement, AVA with a low activity state ('rest') potentiates AVB by tonic acetylcholine transmission and inhibits reversal activity by AVA-A gap junction mediated shunting[26]. (Right panel) During backward movement, AVA with a high activity state (activated) inhibits AVB and potentiates A group neurons by transient acetylcholine transmission. Thus, AVA functions as a master regulator to maintain forward and backward movement and coordinate their transitions.

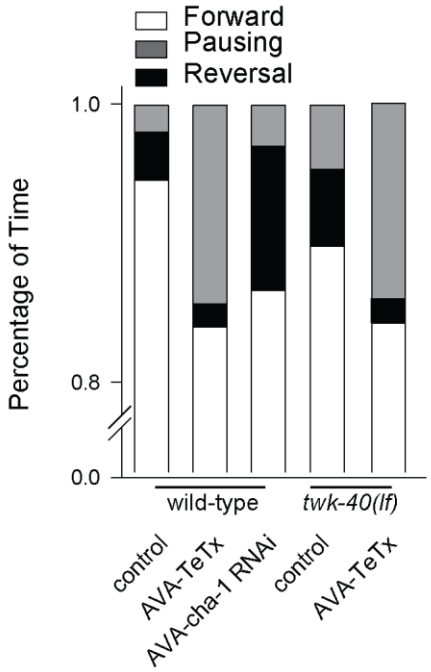

Figure 8S1. Cholinergic signaling from AVA contributes reversal activity

The propensity of movement in each genotype, showing AVA-TeTx impairs the reversal in wild-type (control) (n=18) and *twk-40(lf)* background mutants (n=14) compared to wild-type (n=20) and *twk-40(lf)* (n=21). AVA- specific *cha-1* RNAi (n=14) has a similar effect on the reversal movement as AVA-TeTx.

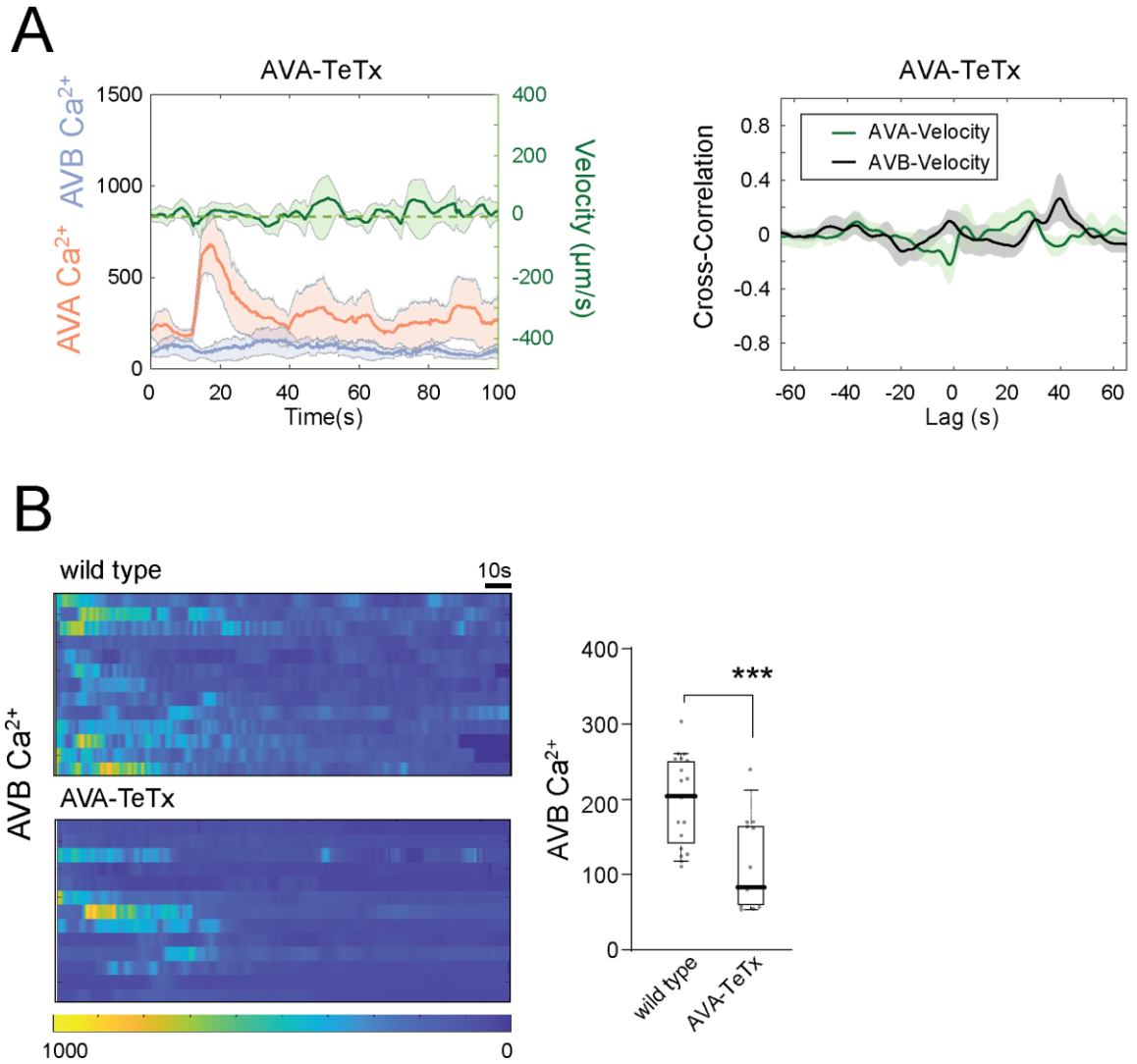

Figure 8S2. TeTx attenuates AVA's constitutive potentiation on forward movement .

A. (Left panel) Velocity and GCaMP traces of AVA and AVB in AVA-TeTx animals. (Right panel) Cross-correlation of AVA-velocity, and AVB-velocity showing a reduced correlation between AVA/AVB activity and velocity (WT=19, AVA-TeTx=10).

B. Raster plot and quantification of AVB calcium activity (GCaMP intensity) during all motor states in freely moving animals, in each genotype. Each trace represents one animal. In AVA-specific TeTx animals, overall AVB calcium activity is decreased. AVB calcium activity is significantly decreased in AVA-specific TeTx animals(n=13) compared to wild-type animals (n=20).

Table 1: Reported RMP in *C. elegans* neurons

Neuron class	Neuron	Approximate RMP reported
Sensory neuron	AFD	-40 mV[92,99], -80 mV[86]
Sensory neuron	AWA	-75 mV[86,100]
Sensory neuron	PLM	-60 mV[96]
Sensory neuron	ASE	-55 mV[32] -60mV[101]
Sensory neuron	ASH	-60 mV[88]
Interneuron	AIY	-55 mV[86]
Interneuron	AIA	-80 mV[102]
Premotor interneuron	AVA	-20 to -30 mV[34,35,63]
Premotor interneuron	AVB	-75 to -55 mV (this study)
Premotor interneuron	AVE	-35 mV (S. Gao, unpublished)
sra-11 expressed neuron	unsure	-20 mV[103]
Motor neuron	RMD	-70 mV and -35 mV[35]
Motor neuron	RIM	-40 mV[86]
Enteric motor neuron	DVB	-60 mV[87]
Enteric motor neuron	AVL	-40 mV[87]
Motor neuron	VA5	-70 mV[36]
Motor neuron	VB6	-50 mV[36]
Motor neuron	VD5	-45 mV[36]

Table 2. Strains and constructs used in this study

Strain	Genotype	Methods/Constructs	Description	Figures
Electrophysiology recording strain				
ZM11177	*hpIs860*	pJH4693	*Ptwk-40-eGFP; Pmyo-2-wcherry*	1E, F. 1S1A, B. 3C. 3S2A, B
ZM11207	*twk-40 (bln336); hpIs860*	pJH4693	*twk-40(gf); Ptwk-40-eGFP; Pmyo-2-wcherry*	1E, F. 1S1A, B. 3C. 3S2A, B
ZM11208	*twk-40 (hp834); hpIs860*	pJH4693	*twk-40(lf); Ptwk-40-eGFP; Pmyo-2-wcherry*	1E, F. 1S1A, B. 3C. 3S2A, B
***twk-40* mutants and locomotion characterization**				
ZM8302	*twk-40 (hp834)*	CRISPR/Cas-9	*twk-40(lf)*	2B, C, 2S1C, D
JIP1514	*twk-40 (bln336)*	CRISPR/Cas-9	*twk-40(gf)*	2B, C
JIP1368	*twk-40 (bln282)*	CRISPR/Cas-9	*twk-40::tagRFP::ZF*	2S1B, D
ZM10113	*twk-40 (bln282); hpIs727*	pJH3830	AVA-specific TWK-40(lf) *twk-40::tagRFP::ZF; Prig-3-zif-1 sl2 RFP; Pttx-3-GFP*	2B, C
ZM10066	*hpEx4053*	pJH4203 pJH2673	AVA- specific TWK-40(gf) *Prig-3-loxp stop loxp twk-40(gf)::GFP; Pnmr-1-cre*	2B, C
ZM9662	*twk-40 (hp834); hpEx3905*	pJH4019 pJH2673	TWK-40 AVA specific rescue *twk-40(lf); Prig-3 FRT Stop FRT twk-40::GFP; Pnmr-1-FLP; HygR*	2C
ZM9565	*twk-40 (bln282); hpEx3909*	pJH3748	AVA, AVE, AVG-TWK-40(lf) *twk-40::tagRFP::ZF; Pnmr-1 zif-1 sl2 RFP; Pttx-3-GFP*	2S1D

ZM9567	*twk-40 (bln282); hpEx3908*	pJH3748	DVC-TWK-40(lf) *twk-40::tagRFP::ZF; Pceh-63 zif-1 sl2 RFP; Pttx-3-GFP*	2S1D
ZM9568	*twk-40 (bln282); hpEx3912*	pJH3862	AVA, RIV-TWK-40(lf) *.twk-40::tagRFP::ZF; Pnpr-4 zif-1 sl2 RFP; Pttx-3-GFP*	2S1D
ZM9632	*twk-40 (bln282); hpEx3889*	pJH3775	AVA, AVB, AVE, SAB, SIA-TWK-40(lf) *twk-40::tagRFP::ZF; Pglr-5 zif-1 sl2 RFP; Pttx-3-GFP*	2S1D
ZM9633	*twk-40 (bln282); hpEx3890*	pJH3747	A,B-TWK-40(lf) *twk-40::tagRFP::ZF; Pacr-2(s) zif-1 sl2 RFP; Pttx-3-GFP*	2S1D
ZM9635	*twk-40 (bln282); hpEx3891*	pJH3831	AVE-TWK-40(lf) *twk-40::tagRFP::ZF; Popt-3 zif-1 sl2 RFP; Pttx-3-GFP*	2S1D
ZM9641	*twk-40 (bln282); hpEx3892*	pJH3982	TWK-40(lf) *twk-40::tagRFP::ZF; Prgef-1 zif-1 sl2 eBFP; Pttx-3-GFP*	2S1D
ZM9646	*twk-40 (bln282); hpEx3896*	pJH4012	A,SAB-TWK-40(lf); *twk-40::tagRFP::ZF; Punc-4 zif-1 sl2 RFP; Pttx-3-GFP*	2S1D
ZM9645	*twk-40 (bln282); hpEx3897*	pJH4011	AVB-TWK-40(lf) *twk-40::tagRFP::ZF; Plgc-55 zif-1 sl2 RFP; Pttx-3-GFP*	2S1D
ZM9983	*twk-40 (bln282); hpEx4034*	pJH4034	SIA, SIB-TWK-40(lf) *twk-40::tagRFP::ZF; Pceh-24 zif-1 sl2 RFP; Pmyo-2-RFP*	2S1D
Immunostaining				
ZM10652	*twk-40 (bln282); hpEx4120*	pJH1371	TWK-40(lf) *twk-40::tagRFP::ZF; prgef-1-GPI::YFP*	1C
AVA-GCaMP imaging strains				

ZM8753	*hpIs516*	pJH3478	*Pnmr-1-GCAMP6::SL2 wcherry*	5G
ZM9059	*hpIs580*	pJH3631	*Prig-3-GCaMP6::wcherry*	1S2A, B
ZM9775	*twk-40 (hp834); hpIs580*	pJH3631	*twk-40(lf); Prig-3-GCaMP6::wcherry*	1S2A
ZM9818	*twk-40 (bln336); hpIs580*	pJH3631	*twk-40(gf); Prig-3-GCaMP6::wcherry*	1S2A, B
ZM10044	*twk-40 (hp834); hpIs580; hpEx3905*	pJH3631 pJH4019 pJH2673	TWK-40 AVA rescue *twk-40(lf); Prig-3-GCaMP6::wcherry; Prig-3-FRT stop FRT twk-40; Pnmr-1-FLP; HygR*	1S2A
ZM10283	*twk-40 (bln282); hpIs727; hpIs580*	pJH3830 pJH3898	AVA-specific TWK-40(lf) *twk-40::tagRFP::ZF; Prig-3-GCaMP6::wcherry; Prig-3-zif-1 sl2 rfp*	2S2C
ZM10346	*hpIs580; hpEx4115*	pJH4316 pJH4237	AVA-specific TWK-40(gf) *Prig-3-GCaMP6::wcherry; Pflp-18-loxp twk-40(gf) loxp; Ptwk-40-cre*	2S2C
***nca-1* and *twk-40* mutants and AVA-GCaMP imaging strains**				
ZM8970	*nca-1 (hp102); hpIs580*	pJH3631	*nca-1(gf); Prig-3-GCaMP6::wcherry*	1S2B
ZM10064	*nca-1 (hp102); twk-40 (bln336 bln282); hpIs580*	pJH3631	*nca-1(gf); twk-40(gf)::ZF; Prig-3-GCaMP6::wcherry; Pmyo-2-RFP*	1S2B
AVA and A ablation strains				
ZM10344	*hpIs371; hpEx4114*	pJH2843 pJH4315	AVA/A miniSOG;	2S2A

		pJH4237	*Punc-4- mito::miniSOG sl2 mcherry; Pflp-18-loxp stop loxp mito::miniSOG sl2 mcherry; ptwk-40-cre*	
ZM11234	*twk-40 (hp834); hpEx4114; hpIs371*	pJH2843 pJH4315 pJH4237	AVA/A miniSOG *twk-40(lf); Punc-4-mito::miniSOG sl2 mcherry; Pflp-18-loxp stop loxp mito::miniSOG sl2 mcherry; ptwk-40-cre*	2S2A
PVC, RIM ablation strain				
ZM7054	*hpIs321*	pJH2827	AVA, AVE, AVD, RIM, PVC Mini SOG *Pnmr-1-tomm-20::miniSOG-UrSL-wCherry*	3S1A
RIM ablation strain				
ZM7978	*hpIs327 V*	pJH2829	RIM miniSOG *Pcex-1-tomm-20::miniSOG-UrSL-wCherry*	3S1A
AVA-Specific TeTx and RNAi mutants				
ZM10755	*hpIs814*	pJH4508 pJH4237	*Pflp-18-loxp Stop loxp TeTx::cherry; ptwk-40-cre*	8A. 8S1
ZM11082	*twk-40 (hp834) hpIs814*	pJH4508 pJH4237	*twk-40(lf); Pflp-18-loxp Stop loxp TeTx::cherry; Ptwk-40-cre*	8A
ZM11086	*hpEx4362*	PCR product injection	AVA-specific cha-1 RNAi *Pflp-18-cha-1(sense); Ptwk-40-cha-1 (antisense); Pttx-3-GFP*	8A
AVA-Neuropeptide secretion marker and TeTx strains				
ZM11078	*hpEx4364; hpEx4351*	pJH4506; pJH4677	*Pnpr-4-ins-22::GFP; Pnpr-4-TeTx*	7C
ZM11039	*hpEx4351*	pJH4677	*Pnpr-4-ins-22::GFP*	7C
ZM11085	*hpIs814; hpEx4363*	pJH4508 pJH4237 pJH4687	*Pflp-18-loxp Stop loxp TeTx::cherry; Ptwk-40-cre; Pnpr-4-ins-22::PHluorin*	7B
ZM11084	*hpEx4363*	pJH4687	*Pnpr-4-ins-22::PHluorin*	7B

ZM10040	*hpIs721*	pjh4169 pjh2673	*Prig-3 FRT stop FRT snb-1::gfp; Pnmr-1 FLP*	7A
ZM10786	*hpIs811; hpIs721*	pjh4169 pjh2673 pJH4508 pJH4237	*Prig-3 FRT stop FRT snb-1::gfp; Pnmr-1 FLP;* *Pflp-18-loxp Stop loxp TeTx::cherry; Ptwk-40-cre*	7A
AVA-Chrimson and related strains				
ZM10206	*hpIs758*	pJH4253 pJH4237	*Prig-3-loxp Stop loxp* *Chrimson::wcherry; Ptwk-40-cre*	6B.
ZM11151	*hpIs758;* *hpIs814*	pJH4253 pJH4237 pJH4508	AVA-specific TeTx *Pflp-18-loxp Stop loxp* *TeTx::wcherry; Prig-3-loxp Stop loxp Chrimson::wcherry; Ptwk-40-cre*	8B.
AVA-HisCl and related strains				
ZM9354	*hpIs636*	N/A	*Prig-3::HisCl1::SL2::mCherry*	6C, D
ZM11286	*hpIs636; hpEx4479*	N/A; pJH4783	*Prig-3::HisCl1::SL2::mCherry; Pnpr-4-snb-1::pHluorin*	6E
ZM11287	*hpEx4479*	pJH4783	*Pnpr-4-snb-1::pHluorin*	6F
ZM11284	*twk-40 (bln336); hpEx4479*	pJH4783	*Twk-40(gf); Pnpr-4-snb-1::pHluorin*	6F
ZM11285	*twk-40 (hp834); hpEx4479*	pJH4783	*Twk-40(lf); Pnpr-4-snb-1::pHluorin*	6F
AVA-GtACR2 and related strains				
ZM10806	*hpIs824*	pJH4562 pJH4237	*Pflp-18-loxp Stop loxp* *gtACR2::wcherry; ptwk-40-cre*	2S2B
ZM10538	*hpIs774; hpEx4081*	pJH4293 pJH4217 pJH4237	AVA-specific GtACR2; AVA-AVB GCaMP *Prig-3- loxp Stop loxp* *gtACR2::wcherry; Ptwk-40-cre;* *Ptwk-40-Gcamp::mNeptune*	4B, D. 4SB, D
AVB-specific GtACR2 strain				
ZM10942	*hpEx4292; hpIs774; lin-15*	pJH4609 pJH4237	*Ppdf-1 loxP EBFP loxP gtACR2::wCherry* *Ptwk-40 cre* *Ptwk-40-Gcamp::mNeptune*	4A, C. 4SA, C

		pJH4293		
AVB ablation and related strains				
ZM7297	*hpIs331*	pJH2890	AVB-miniSOG *Plgc-55-mito::miniSOG UrSL wcherry*	3A, 3S1A, B
ZM10327	*twk-40 (bln282); hpIs331, hpIs727*	pJH2890 pJH3830	AVB-miniSOG, AVA-speicific TWK-40(lf) *Plgc-55-mito::miniSOG UrSL wcherry; twk-40::tagRFP::ZF; Prig-3-zif-1 sl2 rfp*	3B
ZM10683	*hpIs768; hpIs331;*	pJH4316 pJH4237 pJH2890	AVB-miniSOG, AVA-speicific TWK-40(gf) *Pflp-18-loxp twk-40(gf)::GFP loxp; Ptwk-40-cre; Plgc-55-mito::miniSOG UrSL wcherry*	3S1B
ZM11173	*hpIs331; hpIs758*	pJH2890 pJH4253 pJH4237	AVB-miniSOG, AVA-Chrimson *Plgc-55-mito::miniSOG UrSL wcherry; Prig-3-loxp Stop loxp Chrimson::wcherry; Ptwk-40-cre*	6SA
ZM11172	*hpIs331; hpIs824*	pJH2890 pJH4562 pJH4237	AVB-miniSOG; AVA-GtACR2 *Plgc-55-mito::miniSOG UrSL wcherry; Pflp-18-loxp Stop loxp gtACR2::wcherry; Ptwk-40-cre*	3S1C
AVA-AVB GCaMP imaging strains				
ZM10767	*hpIs819*	pJH4542	*Ptwk-40-GCaMP T2A nls::mNeptune*	3D, 5B-D. 5SA-D
ZM11014	*twk-40 (bln282);; hpIs819; hpEx3904*	pJH4542 pJH4018 pJH2673	AVA-specific TWK-40(lf) *twk-40::tagRFP::ZF; Prig-3 FRT zif-1 sl2 eBFP FRT; Pnmr-1-FLP; HygR; Ptwk-40-GCaMP T2A nls::mNeptune*	3D, 5B-D. 5SA, B-D

ZM11015	*hpIs768;* *hpIs819*	pJH4316 pJH4237 pJH4542	AVA-specific TWK-40(gf) *Pflp-18-loxp twk-40(gf)::GFP loxp; Ptwk-40-cre; Ptwk-40-GCaMP T2A nls::mNeptune;*	3D, 5E, F. 5SA, D
ZM11034	*hpIs819;* *hpIs810*	pJH4542 pJH4508 pJH4237	AVA-specific TeTx *Ptwk-40-GCaMP T2A nls::mNeptune ; Pflp-18-loxp TeTx::wcherry loxp; Ptwk-40-cre*	8C. 8S2A, B
Notes: *Stop: either stop codon or let-858 that terminates the expression* *Co-injection markers: Pmyo-2-RFP, Pmyo-3-RFP; Pttx-3-GFP, HygR; lin-15*				

Methods

Constructs and strains

See Supplemental Table for a full list of constructs and stains generated and used in this study. Primers and sequences are available upon request. All *C. elegans* strains were cultured on the standard Nematode Growth Medium (NGM) plates seeded with OP50 and maintained at 22 °C unless specified. The wild-type animal refers to the Bristol N2 strain. L4 stage hermaphrodites were used for the experiments unless specified otherwise. The control animal refers to a transgenetic animal in a wild-type background.

Isolation, cloning, and generation of *twk-40* mutants

The first loss of function allele of *twk-40(hp733)* was isolated in a genetic screen based on altered behavior. *hp733* was isolated with exaggerated amplitude in both forward and reverse movement as well as a tendency to form backward coil. Using SNP mapping, *hp733* was mapped to the left arm of chromosome III past the SNP marker W06F12 at -21. Whole genome sequencing was performed, and a single missense mutation (E36K) was identified in t*wk-40*. Injection of fosmids and plasmids containing wild-type *twk-40* coding sequence fully rescued the behavioral change in *hp733*. Subsequently, we generated another loss of function allele in *twk-40(hp834)* using CRISPR gene editing. *hp834* has a 7bp deletion in between exon 1 and the following intron (at base 3378-3384 (GTTCGAG) of T28A8.1b), resulting in a frame-shift mutation of *twk-40* that expresses only the first twelve amino acids of the channel. *hp834* displayed similar but stronger behavioral defects than *hp733* and was easy to be genotyped. We subsequently used *hp834* as the canonical *lf* allele for experiments shown in this study.

Gain of function allele *bln336, L181N* was engineered by CRISPR/Cas9 editing by mutating the 4298-4299 base of T28A8.1b from CT to AA[44]. TWK-40 degradation was generated by a repurposed E3 ligase degradation system[46]. *bln282 (twk-40::tagRFP::ZF)* was generated by CRISPR/Cas9 genome editing to insert an inframe tagRFP::ZF fusion at base pair 5785 at T28A8.1b (*twk-40*)[94].

AVA-specific TWK-40(*lf*) was generated by expressing ZIF in AVA using *rig-3* promoter or *nmr-1*/*rig-3*-promoter combination (*Prig-3 FRT zif-1 sl2 eBFP FRT; Pnmr-1-FLP*) via FRT/FLP recombination system in *bln282 (twk-40::tagRFP::ZF)* background. AVA-specific TWK-40(gf) was generated by expressing TWK-40(L181N)::GFP in AVA by *flp-18*/*twk-40*-promoter combination (*Pflp-18-loxp stop loxp twk-40(gf)::GFP; Ptwk-40-cre*) or via Cre/loxp recombination system in N2 background, or *rig-3*/*nmr-1* promoter combination (*Prig-3-loxp stop loxp twk-40(gf)::GFP; Pnmr-1-cre*) via FRT/FLP recombination system in N2 background. AVA-specific TWK-40 rescue was generated by expressing TWK-40(WT)::GFP in AVA by *rig-3*/*nmr-1*-promoter combination (*Prig-3 FRT Stop FRT twk-40::GFP; Pnmr-1-FLP*) via Cre/loxp recombination system in twk-40(*lf*) background animals.

Locomotion assay

A single L4 animal was collected and transferred to an NGM plate with a thin layer of OP50. After 30 seconds, it was recorded on a tracking microscope using an in-house developed ImageJ plugin. A 3-minute movie of the animals was recorded at 10 fps. At least 10 animals for each genotype were recorded on the same day using the same condition. The movies were analyzed as previously described[26,53]. The animal is equally divided by 33 segments by its centerline along the longitudinal axis. Only the body curvature between adjacent segment in radian was calculated in this study (segments 5-32 out of 33). Velocity was calculated by the displacement of centroid.

Electrophysiology

HEK293 cell expression and electrophysiology recording: HEK293 cell culture conditions include DMEM medium, 10 percent fetal bovine serum, 1 percent double antibody, 5 percent CO2 and 37 °C. TWK-40 cDNA was flanked between BstXI and NheI sites by PCR and cloned into the pCDNA3.1 vector. Transfection and expression of plasmid in HEK293 cells by liposome ExFect2000 (Vazyme, China). After 24 hours, HEK293 cells were patched using 4–6 MΩ-resistant borosilicate pipettes (1B100F-4, World Precision Instruments, USA). Pipettes were pulled by micropipette puller P-1000 (Sutter, USA), and fire-polished by microforge MF-830 (Narishige, Japan). Membrane potential and I-V curve were recorded in the whole-cell configuration by EPC-9 amplifier (HEKA, Germany), using the pulse and processed with Igor Pro (WaveMetrics, USA) and Clampfit 10 software (Axon Instruments, Molecular Devices, USA). Membrane potential was recorded at 0 pA, I-V curve was recorded at a holding potential from –80 mV to 80 mV. Data were digitized at 10–20 kHz and filtered at 2.6 kHz. The pipette solution contains (in mM): KCl 140; $MgCl_2$ 1; EGTA 10; HEPES 10; Na_2ATP 4; pH 7.3 with KOH, ~300 mOsm. The bath solution consists of (in mM): NaCl 140; KCl 3.6; $CaCl_2$ 2.5; $MgCl_2$ 1; pH 7.3 with NaOH, ~310 mOsm. For low intracellular K^+ recording, the pipette solution contains (in mM): KCl 14; CsCl 126; $MgCl_2$ 1; EGTA 10; HEPES 10; Na_2ATP 4; pH 7.3 with KOH, ~300 mOsm. Chemicals were obtained from Sigma unless stated otherwise. Experiments were performed at room temperatures (20–22 °C).

in situ whole-cell patch clamp of C. elegans neurons: Premotor interneurons AVA, AVB whole-cell patch clamp was performed as previously described[26,34] which was modified from previous reports[35,39,104]. Briefly, 1- or 2-day-old hermaphrodite adults were glued (Histoacryl Blue, Braun) to a sylgard-coated cover glass covered with bath solution (Sylgard 184, Dowcorning) under a stereoscopic microscope (M50, Leica). After clearing the viscera by suction through a glass pipette, the cuticle flap was turned and gently glued down using WORMGLU (GluStitch Inc.) to expose the soma of AVA and AVB neurons with GFP marker. Neurons were patched using ~20 MΩ-resistant borosilicate pipettes (1B100F-4; World Precision Instruments). Pipettes were pulled by micropipette puller P-1000 (Sutter) and fire-polished by microforge MF-830 (Narishige). Resting membrane potential was collected in the whole-cell configuration by pulse software with EPC9 amplifier (HEKA, Germany). Potential was recorded at a holding current of 0 pA. Data were digitized at 10 kHz and filtered at 2.6 kHz. The recording pipette solution consisted of: KCl 25 mM; K-Gluconate115 mM; $CaCl_2$ 0.1 mM; $MgCl_2$ 5 mM; BAPTA 1 mM;

HEPES 10 mM; Na_2ATP 5 mM; Na_2GTP 0.5 mM; cAMP 0.5 mM; cGMP 0.5 mM, pH 7.2 with KOH, ~320 mOsm. cGMP and cAMP were included mainly to increase the longevity of the preparation[34,105]. The bath solution consisted of KCl 5 mM; NaCl 150 mM; $CaCl_2$ 5 mM; $MgCl_2$ 1 mM; glucose 10 mM; sucrose 5 mM; HEPES 15 mM, pH 7.3 with NaOH, ~330 mOsm. Dynamic membrane potential was recorded at 0 pA for at least 30 seconds. The background leak currents were recorded at -60 mV. Healthy preparations were selected based on the following criteria: whole-cell capacitance (1-1.5 pF), and steady-state leak current (-20-0 pA at -60mV). Experiments were performed at room temperatures (20-22 °C).

Cell ablation by MiniSOG

Strains expressing miniSOG[106] in AVB, RIM, AVA, A, or AVA/A were generated, and cell ablation was performed by exposing L2 stage animals to blue LED light as described in our previous studies[25,53,79]. Typically, animals were treated with 30-40 min LED blue light and recovered for 1 day. L4 animals were recorded for behavioral analyses. For PVC ablation, transgenic animals that express miniSOG in multiple premotor interneurons, including PVC were generated from Pnmr-1-mito::miniSOG L2 animals were anesthetized by sodium azide and mounted on a 2 percent agarose pad with a coverslip. The tail region was exposed to a blue laser for 30min. Animals were then recovered for one day and L4 animals were recorded for behavior. Only healthy worms were recorded and analyzed. The ablation efficiency was confirmed by the disappearance or distortion of the soma fluorescence and fragmentation of neurites.

Optogenetic stimulation for simultaneous behavioral and calcium imaging

Behavior upon AVA-optogenetic manipulation: AVA-specific Chrimson and GtACR2 were generated by the cre/loxp system. The specificity of AVA GtACR2 was examined by ablation using *Pnmr-1*-miniSOG. The AVA-ablated animal no longer exhibited locomotor inhibition during forward and backward movement. Transgenic animals were cultured on ATR plates in the dark for two generations. Second-generation L4-stage animals were analyzed for behavior and calcium activities. Behaviors upon stimulation: an individual L4-stage animal was transferred to an imaging plate with a thin layer of evenly spread OP50. After 30 seconds, the movement of the animal was tracked during multiple programmed stimulation cycles: 10s pre-stimulation, 10s stimulation, 10s post-stimulation; or, 30 seconds pre-stimulation, 30 seconds stimulation, and 30 seconds post-stimulation. 488nm and 574nm LED light stimulation were applied to inhibit and activate AVA, by activating GtACR2 and Chrimson, respectively.

Constitutive, minimal Chrimson mediated activation: NGM plates were seeded with OP50/ATR mixture (1ml OP50/0.5µl 50µm ATR). Animals were cultured on such plates for at least 1 day for behavior recording. Before recording, animals were treated with 544nm green LED light for up to 5min (Zeiss V16) and followed by 595nm yellow light exposure (Thorlabs) at low intensity (4 out of 63 A.U.) during recording. *Weak GtACR2 mediated inhibition:* NGM plates were seeded with OP50/ATR mixture (1ml OP50/0.5µl 50um ATR). Animals were cultured on such plates for at least 1 day for behavior recording. During stimulation, animals were exposed to 470nm blue LED light at low intensity(4 out of 63 A.U.).

Behavior upon AVB-optogenetic manipulation: L4 Animal of AVB-specific GtACR2 was incubated on -ATR or +ATR (1ml OP50 /5µl 50µM ATR) plates for 2 hours and then subjected to behavior recording upon constant 470nm LED at low intensity (4 out of 63 A.U.) for 800 seconds. All the spontaneous forward and reversal were analyzed by the centroid velocity during the 800-second recording.

Simultaneously calcium recording and optogenetic manipulation: The experiment process was previously described[79]. Briefly, Animals of AVA-specific-GtACR2 or AVB-specific- GtACR2 (incubated on -ATR, or +ATR (1ml OP50 /5µl 50µM ATR) plates for 2 hours) were immobilized on dry agarose pads in M9 buffer and subjected to full spectrum light illumination to achieve calcium imaging and GtACR-2 mediated optogenetic inhibition simultaneously at 10 fps or 20pfs for 6-20 seconds.

Behavior upon chemogenetic manipulation

Animals carrying an extrachromosomal array for *Prig-3* HisCl::mCherry[31] were incubated on 0mM, 2mM, 5mM, or 10mM histamine plates for 1 hour before spontaneous behavior recording and scoring. For touch-induced reversal scoring, animals were harshly touched on the tail region by a worm picker and the reversals response (duration and fraction of reversals) was manually recorded and scored.

Immunofluorescent staining

Mixed stages of animals of *twk-40*::tagRFP::ZF (for determining cell expression) and *twk-40*::tagRFP::ZF; *prgef*-1-GPI::YFP were fixed in 2 percent paraformaldehyde at 4°C for 1 hour and processed as previously described[107]. Primary antibodies against tagRFP (Thermo Fisher Scientific, R10367, rabbit) and GFP (Roche, mouse) were used at 1:500 and 1:200 dilution, respectively. A secondary antibody of goat-anti-rabbit (Alexa Fluor 488) and goat anti-mouse (Alexa Fluor 594) was used at 1:5000 dilution. L4 stage larvae and adults were imaged with a Nikon spinning disk confocal microscope with a 63x objective and reconstructed by maximum intensity projection. Single layers of acquired images from animals co-expressing TWK-40::tagRFP::ZF and GPI::YFP were examined for subcellular colocalization using an ImageJ plugin (JACoP) and Pearson's coefficient is calculated between GFP and RFP signals.

Fluorescence Microscopy

GFP imaging: Images of fluorescently tagged proteins were captured in live L4 worms or immunostained animals. Live worms were immobilized on dry agarose pads in M9 buffer. Fluorescence signals were captured using Nikon Eclipse 90i confocal microscope and Nikon Eclipse T12 with Yokogawa CSU-X1 spinning disk field scanning confocal system.

Phluorin imaging: images were acquired in live L4 animals. Live animals were immobilized on dry agarose pads in M9 buffer. All the images were acquired within 10min after dry pad preparation by Nikon Eclipse T12 with Yokogawa CSU-X1 spinning disk field scanning confocal system.

All fluorescent images were analyzed by the in-house developed puncta analyzer[108] or ImageJ intensity analyzer.

Free-moving calcium imaging and post analysis

AVA or AVB single neuron imaging was performed in L4 stage animals as previously described[70]. Briefly, an individual transgenic animal was placed on 2.5 percent agarose gel, to ensure its slow movement. The animal was allowed to recover for 3min and then recorded using Zeiss Axioskop 2 Plus upright microscope with 40x objective or Nikon spinning disc confocal with 20x objective in the wide-field mode. A single plane was imaged and recorded by manual tracking and refocusing. GCaMP activity (GCaMP/RFP ratio unless stated otherwise) was obtained as previously described[79].

AVA and AVB co-imaging: An individual transgenic L4 stage animal expressing the GCaMP6s calcium sensor in AVA and AVB (*hpIs819*) was mounted on a 2 percent NGM gel pad with ~1µl M9 buffer so that it could move under a coverslip. Mounted animals were allowed to recover for 3min on the pad before recording. The recording was performed using a 20x objective on Nikon spinning disk confocal microscope. Animals were centered in the field of view by manual tracking. AVB soma was manually kept in focus at the RFP channel during recording.

Velocity and AVA-AVB GCaMP activity (GCaMP intensity) during reversal to forward locomotion transition were subtracted and aligned by house-developed Matlab scripts[79].

Cell-specific perturbation of neurotransmission

AVA-specific TeTx was achieved by the cre-loxp recombination system. AVA-specific *cha-1*RNAi was generated using the combination of P*flp-18* and *Ptwk-40* promoter combination to drive the sense and anti-sense strand of *cha-1* genomic DNA, respectively. The following primers and templates were used: (A) *Pflp-18*: OZM6199 (GATGGATACGCTAACAACTTGG) and OZM6200 (CTACAACGGCAGCGTATTCGATCCCGTCTAAC-CCTGAAA) amplified from pJH4631. (B) *cha-1* exon: OZM6201 (GAATACGCTGCCGTTGTAG) and OZM6240 (GTCGAGTGCTCTATGCACAACC), amplified from N2 genomic DNA. (C) *Ptwk-40*: OZM6199 (GATGGATACGCTAACAACTTGG) and OZM6253 (GTATGATGCGACTATTCAGCTGT-GAATATTCATCACTCGATATTCCA) amplified from pJH4608. (D) *cha-1* exon: OZM6201 (GAATACGCTGCCGTTGTAG) and OZM6202 (CAGCTGAATAGTCGCATCATAC), amplified from N2 genomic DNA. PCR fusion was performed to obtain sense and anti-sense *cha-1* by following primers*: Pflp-18-cha-1*(sense): OZM6203 (AGCTTAGCCGGAATAGGGTCA) and OZM6202 (CAGCTGAATAGTCGCATCATAC), amplified from mixed PCR product (A+B). Ptwk-40-cha-1(antisense): OZM3543 (AATGCGGCCGCTCTAATCACTATCACGT GGGATCTGGATAA); OZM6254 (CGTAG-GCCAGAAAGCCTCAC) from mixed PCR product (C+D). Mixed PCR products were injected into N2 animals.

Modeling

Our approach is to find the simplest phenomenological model (i.e. a model with as few free parameters as possible) that explains the observed calcium activity patterns of AVA and AVB, as opposed to a detailed, more biologically realistic model. A more realistic model will have several parameters, the estimation of which will require assumptions or experiments to fix.

We first note that our experiments suggest that the communication between AVB and AVA is largely unidirectional, with AVA affecting AVB's activity and very little effect in the opposite direction. Consequently, we start with the following equation for the calcium activity of AVB, x_{AVB}

$$\frac{dx_{AVB}}{dt} = -\tau_{AVB} \cdot x_{AVB} + \sigma(w_{AVA} \cdot x_{AVA} + \Sigma_i w_i z_i)$$

Where x_{AVA} is the calcium activity of AVA, z_i is the activity of all other input neurons of AVB, w_i is the synaptic weight of each input and σ denotes the activation function for the dynapse. Typically, the activation function is a sigmoidal function. However, to simplify the model we restrict our attention to the linear case, where σ is simply the identity function, $\sigma(x) = x$.

Next, we make a key simplification to the model above based on our experiments. Our results show that AVA forms the dominant input on to AVB. Specifically, AVA-TWK-40 (gf) animals cannot sustain their forward motion (Fig. 2B) and AVB's calcium is significantly reduced in this background (Fig. 3D). This suggests that we can ignore the input from other neurons. Thus, we set $w_i = 0$ for all neurons other than AVA. Giving us the following leaky-integrator differential equation.

$$\frac{1}{w_{AVA}} \frac{dx_{AVB}}{dt} = -\frac{\tau_{AVB}}{w_{AVA}} \cdot x_{AVB} + x_{AVA}$$

As a final simplification, we assume that the direct input from AVA is faster than the kinetics of the calcium sensor, such that any activity in AVA is immediately reflected in AVB. Thus, we consider the limit $\frac{1}{w_{AVA}} \to 0$. Giving us the final simplified model as,

$$x_{AVB} = a \cdot x_{AVA}$$

Where $a = \frac{w_{AVA}}{\tau_{AVB}}$ is a dimensionless multiplier. As seen in Fig. 5B, this model with $a < 0$ (black dotted line) can predict the anticorrelated activity pattern between AVA and AVB during a reversal, but is unable to explain AVB's activity after the reversal.

To capture the slow decay of AVB, we add an additional slower input from AVA to AVB (as shown in the schematic in Fig. 5A). Giving us the following system of equations with just three free parameters.

$$x_{AVB} = a \cdot x_{AVA} + b \cdot y$$

$$\frac{dy}{dt} = -\tau \cdot y + x_{AVA}$$

Where, a and b are the coefficients for the fast and slow inputs respectively, and τ is the integration timescale for the slow component of AVA. To fit the parameters from calcium imaging data, we used *tfest* function from Matlab's system identification toolbox, which estimates the transfer function for the equation above. Laplace transforming the system of equations above results in the following transfer function,

$$\frac{X_{AVB}(s)}{X_{AVA}(s)} = \left[\frac{a \cdot s + (a \cdot \tau + b)}{s + \tau}\right]$$

which has one zero and one pole. The number of zeros and poles form the input to *tfest* function, along with the calcium traces of AVB calcium (set as output signal) and AVA calcium (set as the input signal). To get a distribution over model parameters and performances, we do a cross-validation procedure where the parameters are estimated from a single recording and then tested on the remaining recordings. The model R-squared showed in Fig 5C shows the distribution from the models thus estimated.

The same setup was used to model the velocity from AVA's calcium activity (Fig 5G) using *tfest* (i.e. a single pole, single zero transfer function), with AVA's activity being set as the input signal and velocity forming the output signal.

Statistical analyses

Electrophysiological analyses: The cumulative distributions for the membrane potential of AVA and AVB were calculated using MATLAB's *ecdf* function. The compute the joint histogram (Fig. 1S1, Fig. 3S2), we first computed the derivative of membrane potential with a finite difference (preceded by smoothing with a Gaussian kernel) and then used MATLAB's bivariate histogram *histogram2* to perform the histogram estimation.

Behavior and fluorescent analysis: Mann-Whitney U tests were used to quantify data of box and whisker plots unless stated otherwise.

Calcium imaging: Error bars in Fig. 4 and Fig. 4S were computed as a 95% confidence interval of the mean bootstrapped over 1000 resamples.

Conflict of interests

The authors have declared that no conflict of interests exist.

Author contributions

Conception and supervision: MZ; Design of experiments, modeling and analyses: MJ, TA, SG, TB, MZ; Data collection and analyses: MJ, TA, BY, WH, ZY, SM, SG; Scripts: TA, QW; MJ, TA and MZ wrote the manuscript; all authors edited, read or approved the manuscript.

Acknowledgments

We thank Ying Wang and Yan Li for technical support; comments and discussions with Ben Mulcahy, Miriam Goodman, and Cori Bargmann. We appreciate funding support from the CIHR.

References

1. Carreira-Rosario, A. *et al.* MDN brain descending neurons coordinately activate backward and inhibit forward locomotion. *Elife* **7**, (2018).

2. Briggman, K. L. & Kristan, W. B. Imaging dedicated and multifunctional neural circuits generating distinct behaviors. *J. Neurosci.* **26**, 10925–10933 (2006).

3. Mazzucato, L. Neural mechanisms underlying the temporal organization of naturalistic animal behavior. *Elife* **11**, (2022).

4. Briggman, K. L. & Kristan, W. B. Multifunctional pattern-generating circuits. *Annual Review of Neuroscience* **31**, 271–294 (2008).

5. Ramirez, J. M. & Pearson, K. G. Generation of motor patterns for walking and flight in motoneurons supplying bifunctional muscles in the locust. *J. Neurobiol.* **19**, 257–282 (1988).

6. Roberts, W. M. *et al.* A stochastic neuronal model predicts random search behaviors at multiple spatial scales in C. elegans. *Elife* **5**, (2016).

7. Berkowitz, A. Both shared and specialized spinal circuitry for scratching and swimming in turtles. *J. Comp. Physiol. A. Neuroethol. Sens. Neural. Behav. Physiol.* **188**, 225–234 (2002).

8. Gaudry, Q., Ruiz, N., Huang, T., Kristan, W. B. & Kristan, W. B. Behavioral choice across leech species: chacun à son goût. *J. Exp. Biol.* **213**, 1356–1365 (2010).

9. Koyama, M. *et al.* A circuit motif in the zebrafish hindbrain for a two alternative behavioral choice to turn left or right. *Elife* **5**, (2016).

10. Popescu, I. R. & Frost, W. N. *Highly Dissimilar Behaviors Mediated by a Multifunctional Network in the Marine Mollusk Tritonia diomedea*. *Soc Neuroscience* (2002).

11. Soffe, S. R. Two distinct rhythmic motor patterns are driven by common premotor and motor neurons in a simple vertebrate spinal cord. *J. Neurosci.* **13**, 4456–4469 (1993).

12. Itti, L. & Koch, C. Computational modelling of visual attention. *Nat. Rev. Neurosci.* **2**, 194–203 (2001).

13. Goodhill, G. J. Contributions of theoretical modeling to the understanding of neural map development. *Neuron* **56**, 301–311 (2007).

14. Kohonen, T. Self-organized formation of topologically correct feature maps. *Biol. Cybern.* **43**, 59–69 (1982).

15. Lynch MIT, N., Musco, C. & Parter, M. Winner-Take-All Computation in Spiking Neural Networks. (2019). doi:10.48550/arxiv.1904.12591

16. Chen, Y. Mechanisms of winner-take-all and group selection in neuronal spiking networks. *Front. Comput. Neurosci.* **11**, 20 (2017).

17. Szigeti, B., Deogade, A. & Webb, B. Searching for motifs in the behaviour of larval Drosophila melanogaster and Caenorhabditis elegans reveals continuity between behavioural states. *J. R. Soc. Interface* **12**, (2015).

18. Stephens, G. J., Johnson-Kerner, B., Bialek, W. & Ryu, W. S. Dimensionality and dynamics in the behavior of C. elegans. *PLoS Comput. Biol.* **4**, (2008).

19. Gomez-Marin, A., Stephens, G. J. & Brown, A. E. X. Hierarchical compression of Caenorhabditis elegans locomotion reveals phenotypic differences in the organization of behaviour. *J. R. Soc. Interface* **13**, (2016).

20. Ahamed, T., Costa, A. C. & Stephens, G. J. Capturing the continuous complexity of behaviour in Caenorhabditis elegans. *Nat. Phys.* **17**, 275–283 (2021).

21. Lindén, H., Petersen, P. C., Vestergaard, M. & Berg, R. W. Movement is governed by rotational neural dynamics in spinal motor networks. *Nat. 2022 6107932* **610**, 526–531 (2022).

22. CROLL, N. A. Components and patterns in the behaviour of the nematode Caenorhabditis elegans. *J. Zool.* **176**, 159–176 (1975).

23. White, J., Southgate, E. & Thomson, J. The structure of the nervous system of the nematode Caenorhabditis elegans. *Trans R Soc L. B Biol ...* (1986).

24. Chen, B. L., Hall, D. H. & Chklovskii, D. B. Wiring optimization can relate neuronal structure and function. *Proc. Natl. Acad. Sci. U. S. A.* **103**, 4723–4728 (2006).

25. Gao, S. *et al.* Excitatory motor neurons are local oscillators for backward locomotion. *Elife* **7**, (2018).

26. Kawano, T. *et al.* An imbalancing act: Gap junctions reduce the backward motor circuit activity to bias C. elegans for forward locomotion. *Neuron* **72**, 572–586 (2011).

27. Xu, T. *et al.* Descending pathway facilitates undulatory wave propagation in Caenorhabditis elegans through gap junctions. *Proc. Natl. Acad. Sci. U. S. A.* **115**, E4493–E4502 (2018).

28. Fang-Yen, C., Alkema, M. J. & Samuel, A. D. T. Illuminating neural circuits and behaviour in *Caenorhabditis elegans* with optogenetics. *Philos. Trans. R. Soc. B Biol. Sci.* **370**, 20140212 (2015).

29. Chalfie, M. *et al.* The neural circuit for touch sensitivity in Caenorhabditis elegans. *J. Neurosci.* **5**, 956–964 (1985).

30. Rodgers, J. B. & Ryu, W. S. Targeted thermal stimulation and high-content phenotyping reveal that the C. elegans escape response integrates current behavioral state and past experience. *PLoS One* **15**, (2020).

31. Pokala, N., Liu, Q., Gordus, A. & Bargmann, C. I. Inducible and titratable silencing of Caenorhabditis elegans neurons in vivo with histamine-gated chloride channels. *Proc. Natl. Acad. Sci.* **111**, 2770–2775 (2014).

32. Goodman, M. B., Hall, D. H., Avery, L. & Lockery, S. R. Active currents regulate

sensitivity and dynamic range in C. elegans Neurons. *Neuron* **20**, 763–772 (1998).

33. Goodman, M. B., Lindsay, T. H., Lockery, S. R. & Richmond, J. E. Electrophysiological Methods for C. elegans Neurobiology. *Methods Cell Biol.* **107**, 409 (2012).

34. Xie, L. *et al.* NLF-1 Delivers a Sodium Leak Channel to Regulate Neuronal Excitability and Modulate Rhythmic Locomotion. *Neuron* **77**, 1069–1082 (2013).

35. Mellem, J., Brockie, P., Madsen, D. & Maricq, A. Action potentials contribute to neuronal signaling in C. elegans. *Nat. Neurosci.* (2008).

36. Liu, P., Chen, B. & Wang, Z.-W. SLO-2 potassium channel is an important regulator of neurotransmitter release in Caenorhabditis elegans. *Nat. Commun. 2014 51* **5**, 1–12 (2014).

37. Huang, Y. C. *et al.* Gain-of-function mutations in the UNC-2/CaV2α channel lead to excitation-dominant synaptic transmission in C. elegans. *Elife* **8**, (2019).

38. Saheki, Y. & Bargmann, C. I. Presynaptic CaV2 calcium channel traffic requires CALF-1 and the alpha(2)delta subunit UNC-36. *Nat. Neurosci.* **12**, 1257–1265 (2009).

39. Richmond, J. E. & Jorgensen, E. M. One GABA and two acetylcholine receptors function at the C. elegans neuromuscular junction. *Nat. Neurosci.* **2**, 791–798 (1999).

40. Oh, K. H., Krout, M. D., Richmond, J. E. & Kim, H. UNC-2 CaV2 Channel Localization at Presynaptic Active Zones Depends on UNC-10/RIM and SYD-2/Liprin-α in Caenorhabditis elegans. *J. Neurosci.* **41**, 4782–4794 (2021).

41. Lesage, F. TWIK-1, a ubiquitous human weakly inward rectifying K+ channel with a novel structure. *EMBO J.* **15**, 1004–1011 (1996).

42. Cluzeaud, F. *et al.* Expression of TWIK-1, a novel weakly inward rectifying potassium channel in rat kidney. *Am. J. Physiol. - Cell Physiol.* **275**, (1998).

43. Chavez, R., Gray, A., Zhao, B. & Kindler, C. TWIK-2, a new weak inward rectifying member of the tandem pore domain potassium channel family. *J. Biol.* (1999).

44. Ben Soussia, I. *et al.* Mutation of a single residue promotes gating of vertebrate and invertebrate two-pore domain potassium channels. *Nat. Commun.* **10**, 1–13 (2019).

45. Aryal, P., Abd-Wahab, F., Bucci, G. & Sansom, M. A hydrophobic barrier deep within the inner pore of the TWIK-1 K2P potassium channel. *Nature* (2014).

46. Armenti, S. T., Lohmer, L. L., Sherwood, D. R. & Nance, J. Repurposing an endogenous degradation system for rapid and targeted depletion of C. elegans proteins. *Dev.* **141**, 4640–4647 (2014).

47. Zheng, Y., Brockie, P. J., Mellem, J. E., Madsen, D. M. & Maricq, A. V. Neuronal control of locomotion in C. elegans is modified by a dominant mutation in the GLR-1 ionotropic glutamate receptor. *Neuron* **24**, 347–361 (1999).

48. Pirri, J. K., McPherson, A. D., Donnelly, J. L., Francis, M. M. & Alkema, M. J. A Tyramine-Gated Chloride Channel Coordinates Distinct Motor Programs of a

Caenorhabditis elegans Escape Response. *Neuron* **62**, 526–538 (2009).

49. Ji, N. *et al.* Corollary discharge promotes a sustained motor state in a neural circuit for navigation. *Elife* **10**, (2021).

50. Gordus, A., Pokala, N., Levy, S., Flavell, S. W. & Bargmann, C. I. Feedback from network states generates variability in a probabilistic olfactory circuit. *Cell* **161**, 215–227 (2015).

51. Wagh, D. A. *et al.* Bruchpilot, a protein with homology to ELKS/CAST, is required for structural integrity and function of synaptic active zones in Drosophila. *Neuron* **49**, 833–844 (2006).

52. Sordillo, A. & Bargmann, C. I. Behavioral control by depolarized and hyperpolarized states of an integrating neuron. *Elife* **10**, (2021).

53. Chitturi, J. *et al.* The UBR-1 ubiquitin ligase regulates glutamate metabolism to generate coordinated motor pattern in Caenorhabditis elegans. *PLOS Genet.* **14**, e1007303 (2018).

54. Fouad, A. D. *et al.* Distributed rhythm generators underlie Caenorhabditis elegans forward locomotion. *Elife* **7**, (2018).

55. Gao, S. *et al.* The NCA sodium leak channel is required for persistent motor circuit activity that sustains locomotion. *Nat. Commun.* **6**, 6323 (2015).

56. Kato, S. *et al.* Global Brain Dynamics Embed the Motor Command Sequence of Caenorhabditis elegans. *Cell* **163**, 656–669 (2015).

57. Kindt, K. S. *et al.* Dopamine Mediates Context-Dependent Modulation of Sensory Plasticity in C. elegans. *Neuron* **55**, 662–676 (2007).

58. Nguyen, J. P. *et al.* Whole-brain calcium imaging with cellular resolution in freely behaving *Caenorhabditis elegans*. *Proc. Natl. Acad. Sci.* **113**, E1074–E1081 (2016).

59. N, J. *et al.* Corollary discharge promotes a sustained motor state in a neural circuit for navigation. *Elife* **10**, (2021).

60. Ben Arous, J., Tanizawa, Y., Rabinowitch, I., Chatenay, D. & Schafer, W. R. Automated imaging of neuronal activity in freely behaving Caenorhabditis elegans. *J. Neurosci. Methods* **187**, 229–234 (2010).

61. Venkatachalam, V. *et al.* Pan-neuronal imaging in roaming Caenorhabditis elegans. *Proc. Natl. Acad. Sci. U. S. A.* **113**, E1082–E1088 (2016).

62. Schmitt, C., Schultheis, C., Husson, S. & Liewald, J. Specific expression of channelrhodopsin-2 in single neurons of Caenorhabditis elegans. *PLoS One* (2012).

63. Liu, P., Chen, B., Mailler, R. & Wang, Z. W. Antidromic-rectifying gap junctions amplify chemical transmission at functionally mixed electrical-chemical synapses. *Nat. Commun.* **8**, 1–16 (2017).

64. Starich, T. A., Xu, J., Skerrett, I. M., Nicholson, B. J. & Shaw, J. E. Interactions between innexins UNC-7 and UNC-9 mediate electrical synapse specificity in the Caenorhabditis

elegans locomotory nervous system. *Neural Dev. 2009 41* **4**, 1–28 (2009).

65. Bhardwaj, A., Thapliyal, S., Dahiya, Y. & Babu, K. FLP-18 functions through the G-protein-coupled receptors NPR-1 and NPR-4 to modulate reversal length in Caenorhabditis elegans. *J. Neurosci.* **38**, 4641–4654 (2018).

66. Taylor, S. R. *et al.* Molecular topography of an entire nervous system. *Cell* **184**, 4329-4347.e23 (2021).

67. Hammarlund, M., Hobert, O., Miller, D. M. & Sestan, N. The CeNGEN Project: The Complete Gene Expression Map of an Entire Nervous System. *Neuron* **99**, 430–433 (2018).

68. Hoogstraaten, R. I., van Keimpema, L., Toonen, R. F. & Verhage, M. Tetanus insensitive VAMP2 differentially restores synaptic and dense core vesicle fusion in tetanus neurotoxin treated neurons. *Sci. Rep.* **10**, (2020).

69. Schiavo, G. G. *et al.* Tetanus and botulinum-B neurotoxins block neurotransmitter release by proteolytic cleavage of synaptobrevin. *Nat. 1992 3596398* **359**, 832–835 (1992).

70. Lim, M. A. *et al.* Neuroendocrine modulation sustains the C. elegans forward motor state. *Elife* **5**, (2016).

71. Hammell, C. M. & Hannon, G. J. Inducing RNAi in Caenorhabditis elegans by Injection of dsRNA. *Cold Spring Harb. Protoc.* **2016**, 80–85 (2016).

72. Ghezzi, A., Liebeskind, B. J., Thompson, A., Atkinson, N. S. & Zakon, H. H. Ancient association between cation leak channels and Mid1 proteins is conserved in fungi and animals. *Front. Mol. Neurosci.* **7**, (2014).

73. Zhao, B., Khare, P., Feldman, L. & Dent, J. A. Reversal Frequency in Caenorhabditis elegans Represents an Integrated Response to the State of the Animal and Its Environment. *J. Neurosci.* **23**, 5319 (2003).

74. Wang, Y. *et al.* Flexible motor sequence generation during stereotyped escape responses. *Elife* **9**, 1–27 (2020).

75. Mohammadi, A., Byrne Rodgers, J., Kotera, I. & Ryu, W. S. Behavioral response of Caenorhabditis elegans to localized thermal stimuli. *BMC Neurosci.* **14**, (2013).

76. Cook, S. J. *et al.* Whole-animal connectomes of both Caenorhabditis elegans sexes. *Nature* **571**, 63–71 (2019).

77. Witvliet, D. *et al.* Connectomes across development reveal principles of brain maturation. *Nature* **596**, 257–261 (2021).

78. Gray, J. M., Hill, J. J. & Bargmann, C. I. A circuit for navigation in Caenorhabditis elegans. *Proc. Natl. Acad. Sci. U. S. A.* **102**, 3184–3191 (2005).

79. Lu, Y. *et al.* Extrasynaptic signaling enables an asymmetric juvenile motor circuit to produce symmetric undulation. *Curr. Biol.* **0**, (2022).

80. Kaplan, H. S., Salazar Thula, O., Khoss, N. & Zimmer Correspondence, M. Nested

Neuronal Dynamics Orchestrate a Behavioral Hierarchy across Timescales. *Neuron* **105**, 562-576.e9 (2020).

81. Randi, F., Sharma, A. K., Dvali, S. & Leifer, A. M. A functional connectivity atlas of $\textit{C. elegans}$ measured by neural activation. (2022). doi:10.48550/arxiv.2208.04790

82. Ashaber, M. *et al.* Anatomy and activity patterns in a multifunctional motor neuron and its surrounding circuits. *Elife* **10**, 1–30 (2021).

83. Takahashi, N., Sasaki, T., Matsumoto, W., Matsuki, N. & Ikegaya, Y. Circuit topology for synchronizing neurons in spontaneously active networks. *Proc. Natl. Acad. Sci. U. S. A.* **107**, 10244–10249 (2010).

84. Wang, Z. *et al.* The relationship of anatomical and functional connectivity to resting state connectivity in primate somatosensory cortex. *Neuron* **78**, 1116 (2013).

85. Zarin, A. A., Mark, B., Cardona, A., Litwin-Kumar, A. & Doe, C. Q. A multilayer circuit architecture for the generation of distinct locomotor behaviors in Drosophila. *Elife* **8**, (2019).

86. Liu, Q., Kidd, P. B., Dobosiewicz, M. & Bargmann, C. I. C. elegans AWA Olfactory Neurons Fire Calcium-Mediated All-or-None Action Potentials. *Cell* **175**, 57-70.e17 (2018).

87. Jiang, J. *et al.* C. elegans enteric motor neurons fire synchronized action potentials underlying the defecation motor program. *Nat. Commun. 2022 131* **13**, 1–15 (2022).

88. Geffeney, S. L. *et al.* DEG/ENaC but not TRP channels are the major mechanoelectrical transduction channels in a C. elegans nociceptor. *Neuron* **71**, 845 (2011).

89. Lindsay, T. H., Thiele, T. R. & Lockery, S. R. Optogenetic analysis of synaptic transmission in the central nervous system of the nematode Caenorhabditis elegans. *Nat. Commun.* **2**, 306 (2011).

90. Liu, Q., Hollopeter, G. & Jorgensen, E. M. Graded synaptic transmission at the Caenorhabditis elegans neuromuscular junction. *Proc. Natl. Acad. Sci. U. S. A.* **106**, 10823–10828 (2009).

91. O'Hagan, R. & Chalfie, M. Mechanosensation in Caenorhabditis elegans. *Int. Rev. Neurobiol.* **69**, 169–203 (2005).

92. Ramot, D., MacInnis, B. L. & Goodman, M. B. Bidirectional temperature-sensing by a single thermosensory neuron in C. elegans. *Nat. Neurosci.* **11**, 908–915 (2008).

93. Salkoff, L., Wei, A., Baban, B., Butler, A. & Fawcett, G. Potassium channels in C. elegans. (2005).

94. El Mouridi, S. *et al.* Reliable CRISPR/Cas9 genome engineering in Caenorhabditis elegans using a single efficient sgRNA and an easily recognizable phenotype. *G3 Genes, Genomes, Genet.* **7**, 1429–1437 (2017).

95. Genome sequence of the nematode C. elegans: a platform for investigating biology.

Science **282**, 2012–2018 (1998).

96. O'Hagan, R., Chalfie, M. & Goodman, M. B. The MEC-4 DEG/ENaC channel of Caenorhabditis elegans touch receptor neurons transduces mechanical signals. *Nat. Neurosci.* **8**, 43–50 (2005).

97. Salkoff, L. *et al.* Evolution tunes the excitability of individual neurons. *Neuroscience* **103**, 853–859 (2001).

98. Zhou, C. *et al.* Differential modulation of C. elegans motor behavior by NALCN and two-pore domain potassium channels. *PLoS Genet.* **18**, (2022).

99. Goodman, M. B. & Sengupta, P. The extraordinary AFD thermosensor of C. elegans. *Pflugers Arch.* **470**, 839 (2018).

100. Nicoletti, M. *et al.* Biophysical modeling of C. Elegans neurons: Single ion currents and whole-cell dynamics of AWCon and RMD. *PLoS One* **14**, e0218738 (2019).

101. Shindou, T. *et al.* Active propagation of dendritic electrical signals in C. elegans. *Sci. Reports 2019 91* **9**, 1–12 (2019).

102. Dobosiewicz, M., Liu, Q. & Bargmann, C. I. Reliability of an interneuron response depends on an integrated sensory state. *Elife* **8**, (2019).

103. Faumont, S., Lindsay, T. & Lockery, S. Neuronal microcircuits for decision making in C. elegans. *Curr. Opin. Neurobiol.* **22**, 580–591 (2012).

104. Richmond, J. E., Davis, W. S. & Jorgensen, E. M. Unc-13 is required for synaptic vesicle fusion in C. elegans. *Nat. Neurosci.* **2**, 959–964 (1999).

105. Brockie, P. J., Mellem, J. E., Hills, T., Madsen, D. M. & Maricq, A. V. The C. elegans Glutamate Receptor Subunit NMR-1 Is Required for Slow NMDA-Activated Currents that Regulate Reversal Frequency during Locomotion. *Neuron* **31**, 617–630 (2001).

106. Qi, Y., Garren, E. & Shu, X. Photo-inducible cell ablation in Caenorhabditis elegans using the genetically encoded singlet oxygen generating protein miniSOG. *Proc.* (2012).

107. Meng, J. *et al.* Myrf ER-bound transcription factors drive C. elegans synaptic plasticity via cleavage-dependent nuclear translocation. *Dev. Cell* **41**, 180 (2017).

108. Yeh, E., Kawano, T., Weimer, R. M., Bessereau, J. L. & Zhen, M. Identification of Genes Involved in Synaptogenesis Using a Fluorescent Active Zone Marker in Caenorhabditis elegans. *J. Neurosci.* **25**, 3833 (2005).